Supporting Information

Switchable Narrow Nonlocal Conducting Polymer Plasmonics

Dongqing Lin[1], Yulong Duan[1], Pravallika Bandaru[1], Pengli Li[1], Mohammad Shaad Ansari[1], Alexander Yu. Polyakov [1], Janna Wilhelmsen[1], Magnus P. Jonsson[1,*]

[1]Laboratory of Organic Electronics, Department of Science and Technology (ITN), Linköping University, Norrköping, SE-60174, Sweden

Part 1 Permittivity and matching conditions of collective lattice resonance (CLR) in square arrays

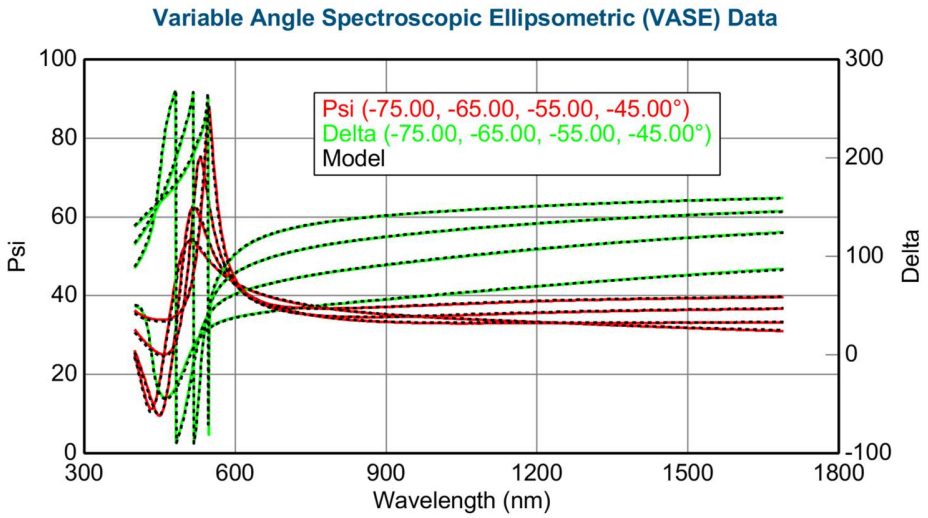

Figure S1. Spectroscopic ellipsometry data (ranging from 210 nm to 1690 nm) for a PEDOT film (acid-treated PEDOT:ToS, with thickness of 200 nm). These raw data and the fitting were processed using the VASE software. The Psi (ψ, marked in the red line) and Delta (Δ, marked in the green line) were acquired at four angles (45° , 55° , 65° , and, 75°). The black dashed lines are the best fitting data by using the Drude-Lorents model.

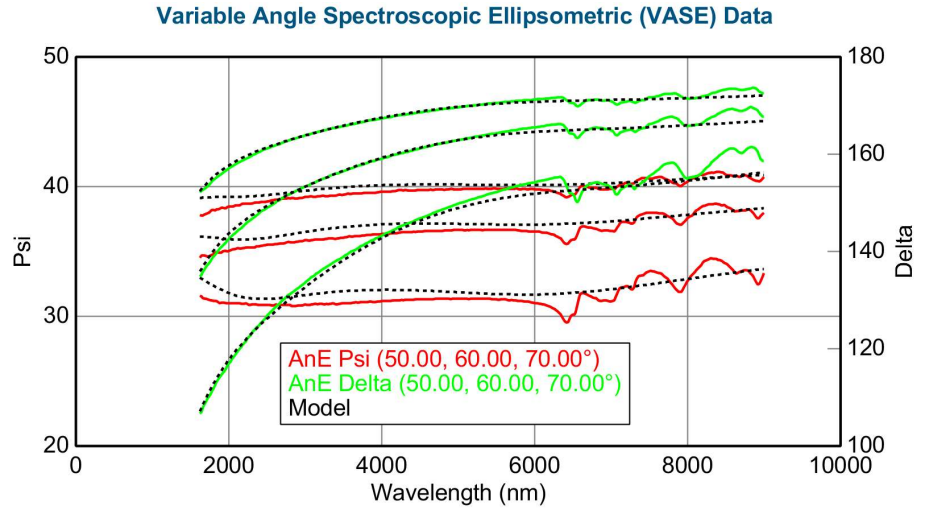

Figure S2. Spectroscopic ellipsometry data (ranging from 1690 nm to 9000 nm) for a PEDOT film (acid-treated PEDOT:ToS, , with thickness of 200 nm). These raw data and the fitting processing are based on the VASE software. The Psi (ψ, marked in the red line) and Delta

(Δ, marked in the green line) are achieved with three angles (50° , 60° , and, 70°). The black dashed lines are shown in the best fitting data by using the Drude-Lorentz model.

Supplemental table 1: Oscillators for oxidized state in the in-plane direction

$\varepsilon_\infty = 1.17$			
Oscillator No. (*j* th)	Frequency ω_j (eV)	Broadening γ_j (eV)	Amplitude A_j (eV^2)
Drude	0	0.32	5.28
1	1.52	1.16	1.69
2	6.08	2.27	3.59
3	10.35	0	128.02

Supplemental table 2: Oscillators for oxidized state in the out-of-plane direction

$\varepsilon_\infty = 1.40$			
Oscillator No. (*j* th)	Frequency ω_j (eV)	Broadening γ_j (eV)	Amplitude A_j (eV^2)
1	0.1	0.91	0.046
2	6.80	3.86	30.32
3	4.53	0.60	0.41
4	0.028	0.16	0.076
5	0.46	0.35	0.31
6	0.025	0.022	0.021
7	12.00	0	135.25

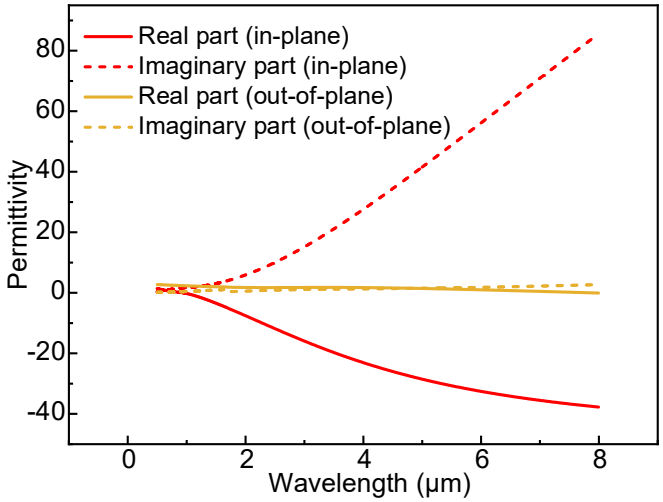

Figure S3. Permittivity of acid-treated PEDOT:ToS (film thickness of 200 nm). These data were obtained from the calculation of Drude-Lorentz model by fitting the data of spectroscopic ellipsometry above.

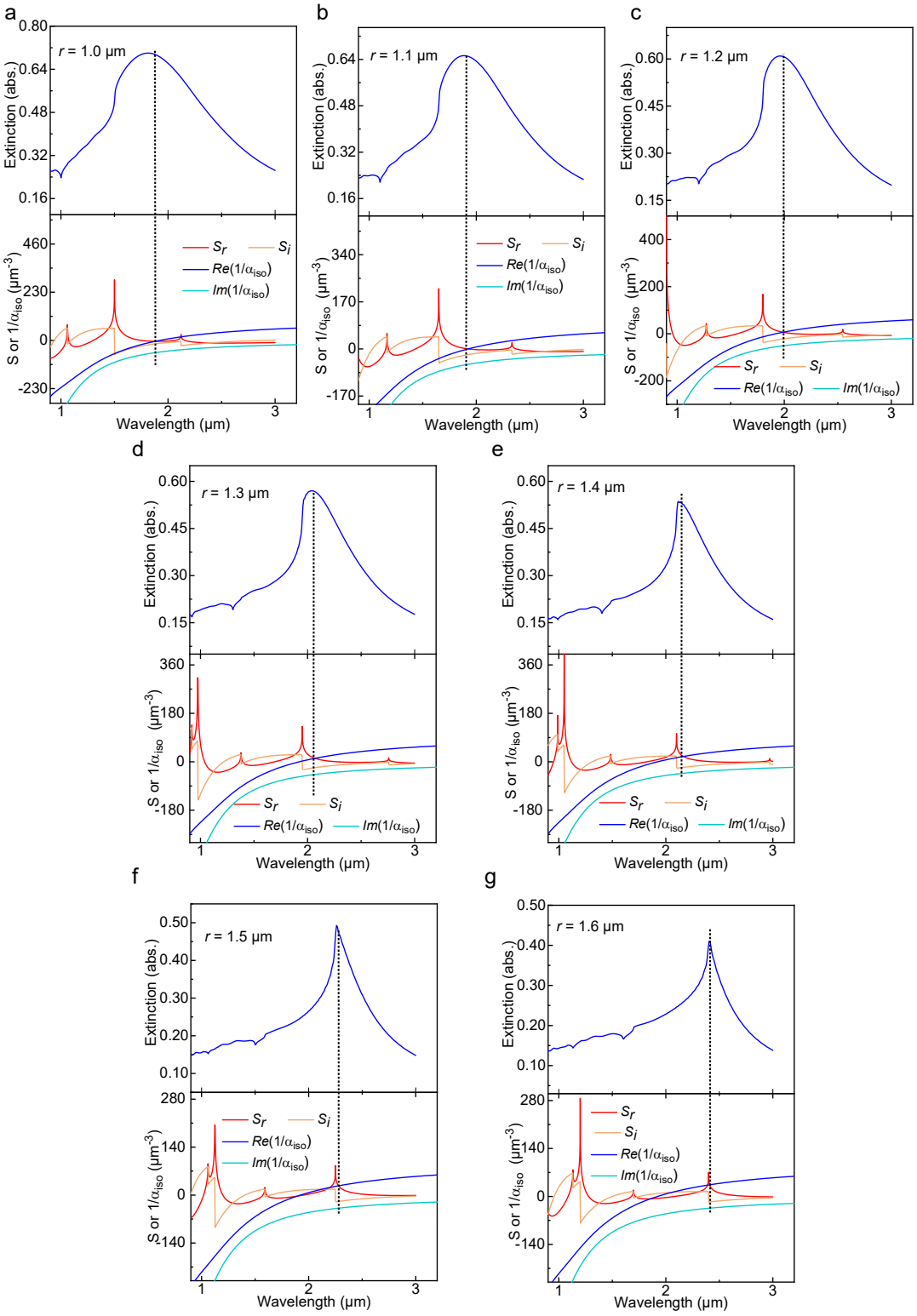

Figure S4. Analysis of array factors and extinction spectra for square arrays with different periodic distances *r* = 1.0-1.6 μm, based on acid-treated PEDOT:ToS. The extinction spectra are

were obtained by FDTD simulations. The diameter of the nanodisks was set to 0.52 μm, and the height of the nanodisks was set to 0.2 μm.

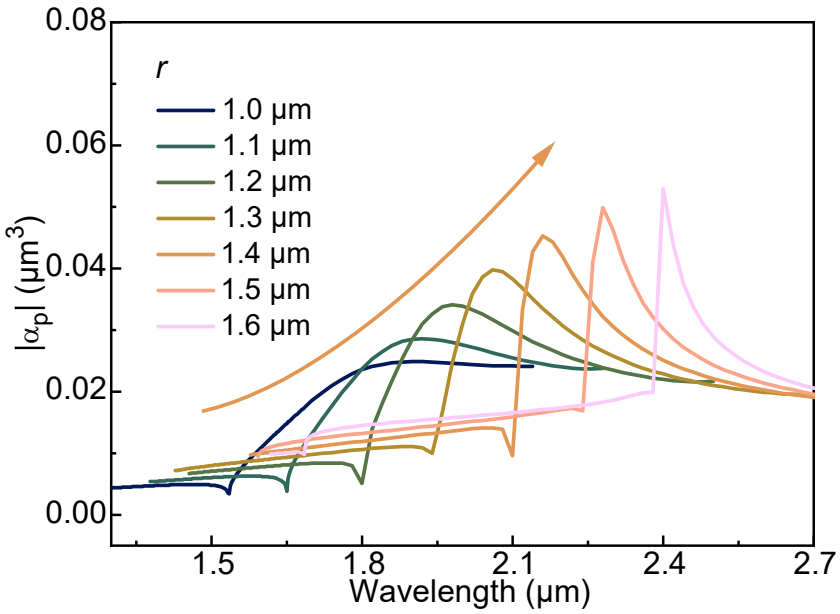

Figure S5. Absolute periodic polarizability $|\alpha_p|$ of square-shaped arrays with different periodic distances *r* = 1.0-1.6 μm, based on acid-treated PEDOT:ToS nanoantennas with 0.52 μm diameter and 0.2 μm height. The peaks correspond to the surface plasmonic resonance based on the coupling interactions along the square-edges.

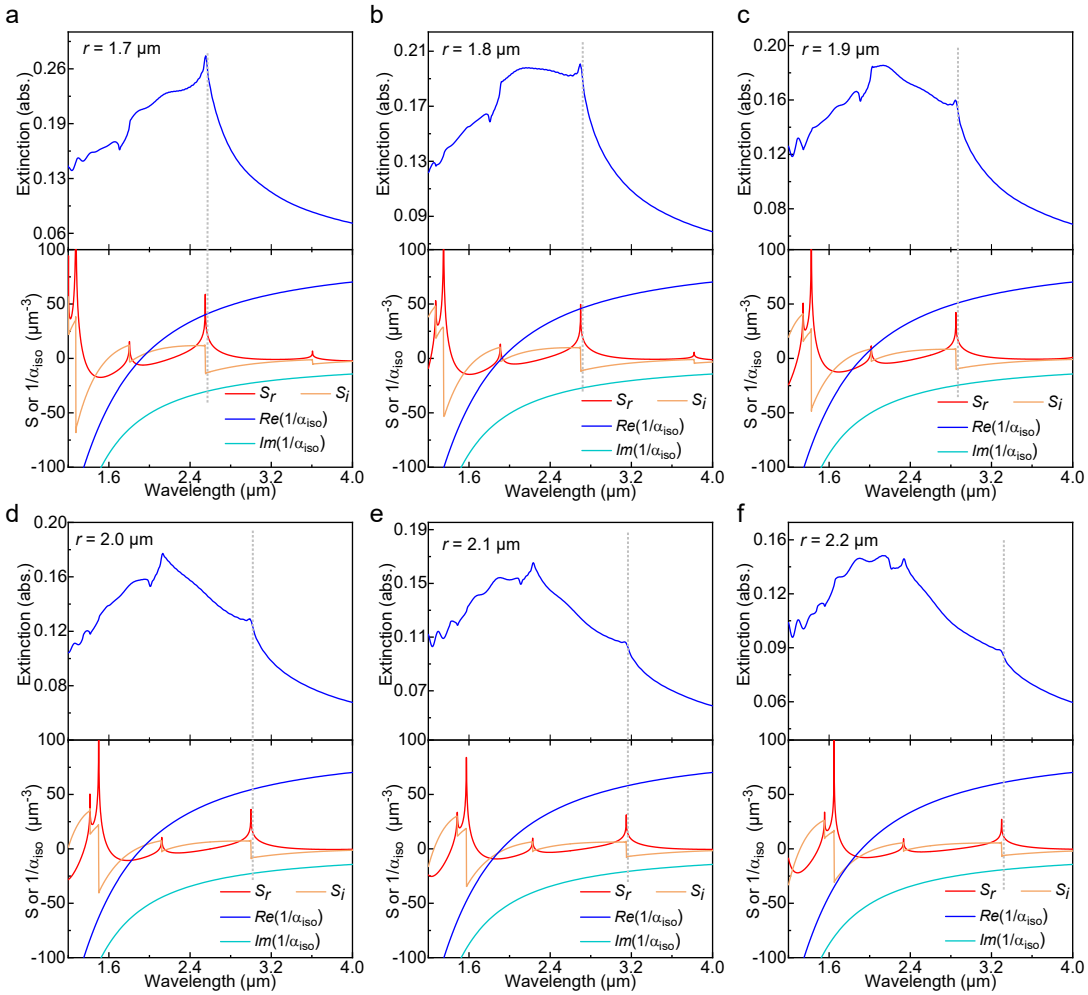

Figure S6. Analysis of array factors and extinction spectra for square arrays with extended periodic distances *r* = 1.7-2.2 μm, based on acid-treated PEDOT:ToS. The extinction spectra are were obtained by FDTD simulations. The diameter of the nanodisks was set to 0.52 μm, and the height of the nanodisks was set to 0.2 μm.

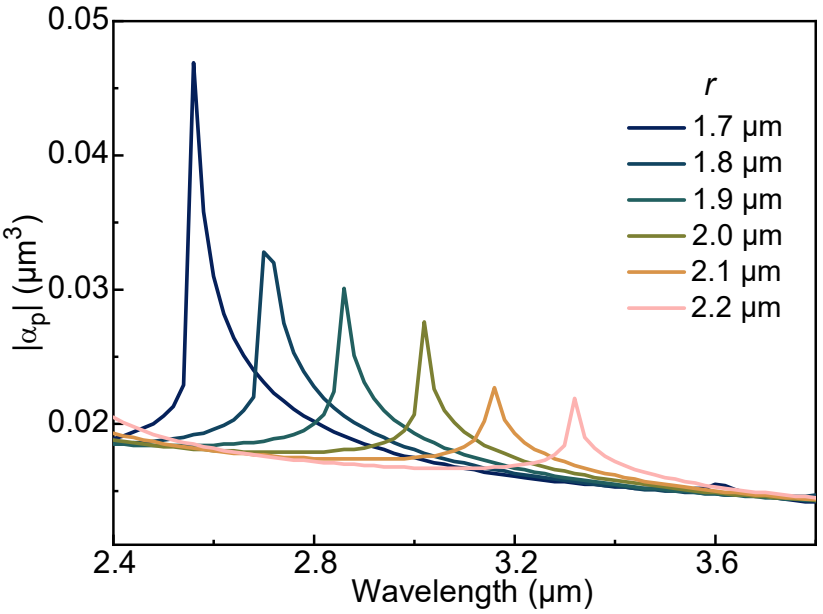

Figure S7. Absolute periodic polarizability $|\alpha_p|$ of square-shaped arrays with extended periodic distances *r* = 1.7-2.2 μm, based on acid-treated PEDOT:ToS nanoantennas with 0.52 μm diameter and 0.2 μm height.

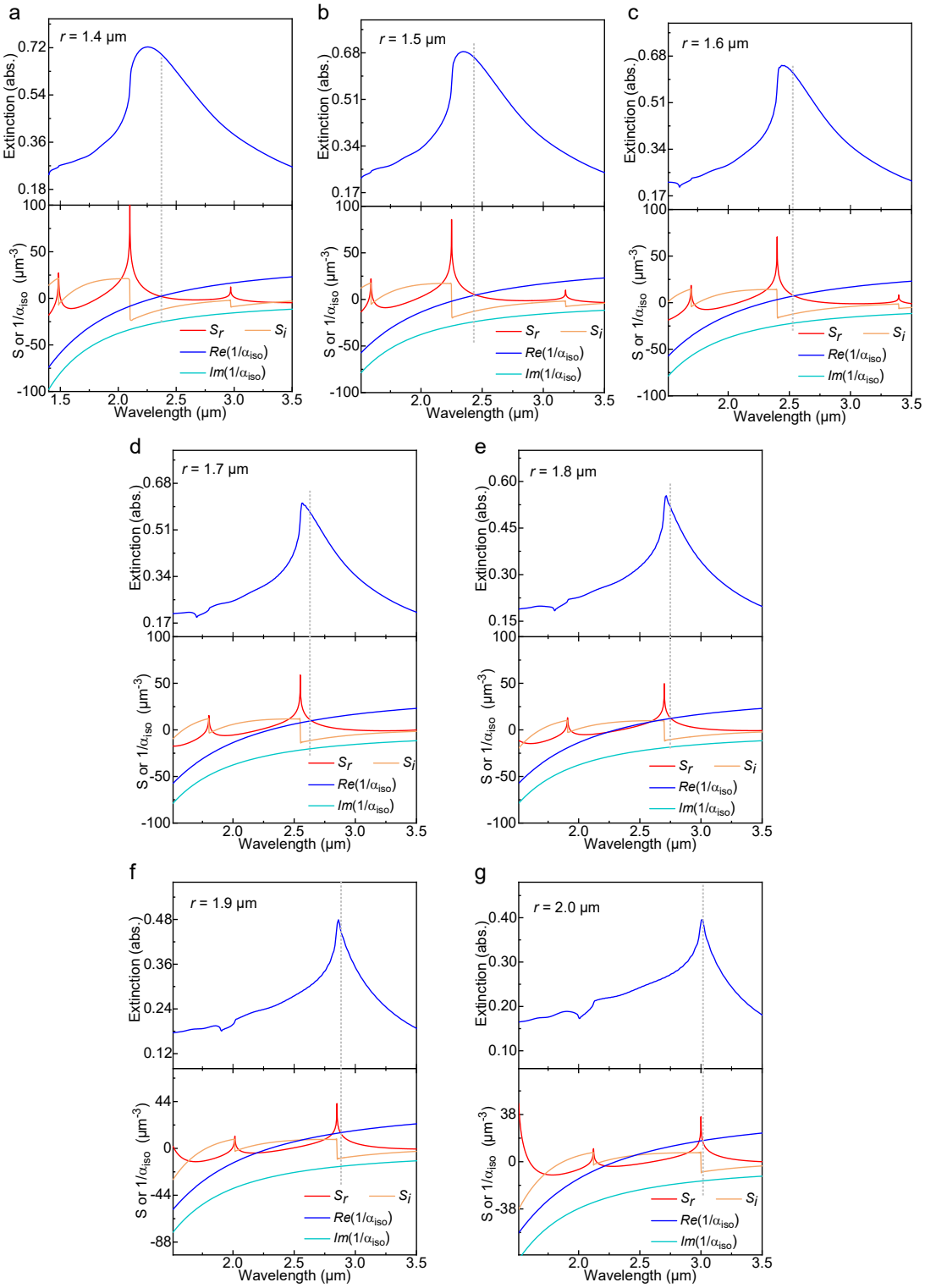

Figure S8. Analysis of array factors and extinction spectra for square arrays with different periodic distances *r* = 1.4-2.0 μm, based on acid-treated PEDOT:ToS. The extinction spectra

were obtained by FDTD simulations. The diameter of the nanodisks was set to 0.70 µm, and the height of the nanodisks was set to 0.2 µm.

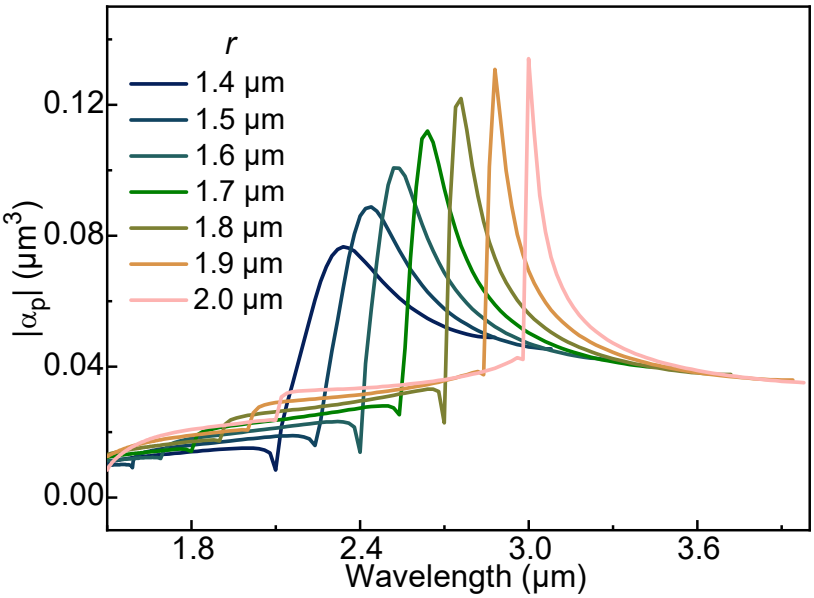

Figure S9. Absolute periodic polarizability $|\alpha_p|$ of square-shaped arrays with different periodic distances *r* = 1.4-2.0 µm, based on acid-treated PEDOT:ToS nanoantennas with 0.70 µm diameter and 0.2 µm height.

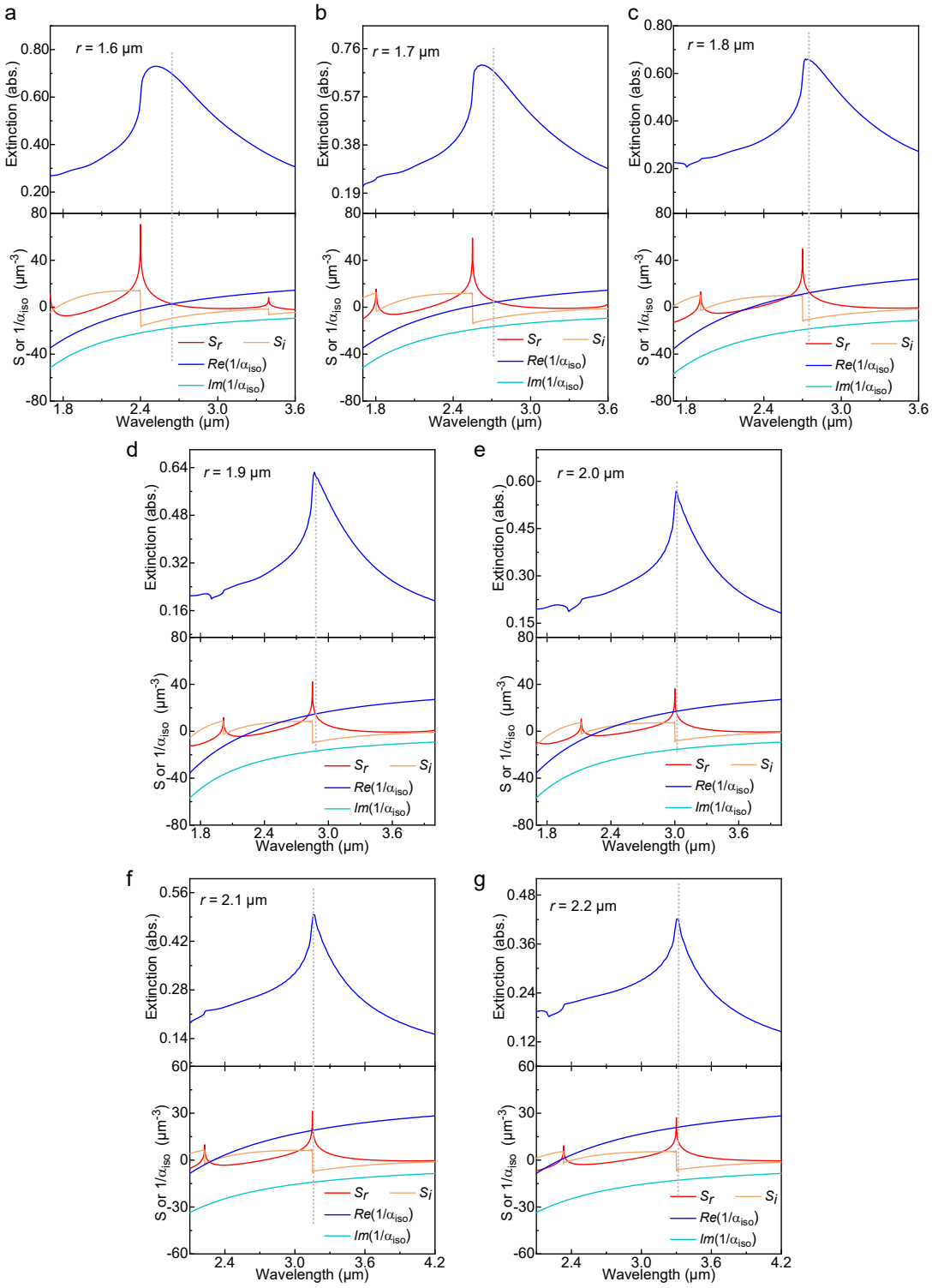

Figure S10. Analysis of array factors and extinction spectra for square arrays with different periodic distances *r* = 1.6-2.2 μm, based on acid-treated PEDOT:ToS. The extinction spectra were obtained by FDTD simulations. The diameter of the nanodisks was set to 0.80 μm, and the height of the nanodisks was set to 0.2 μm.

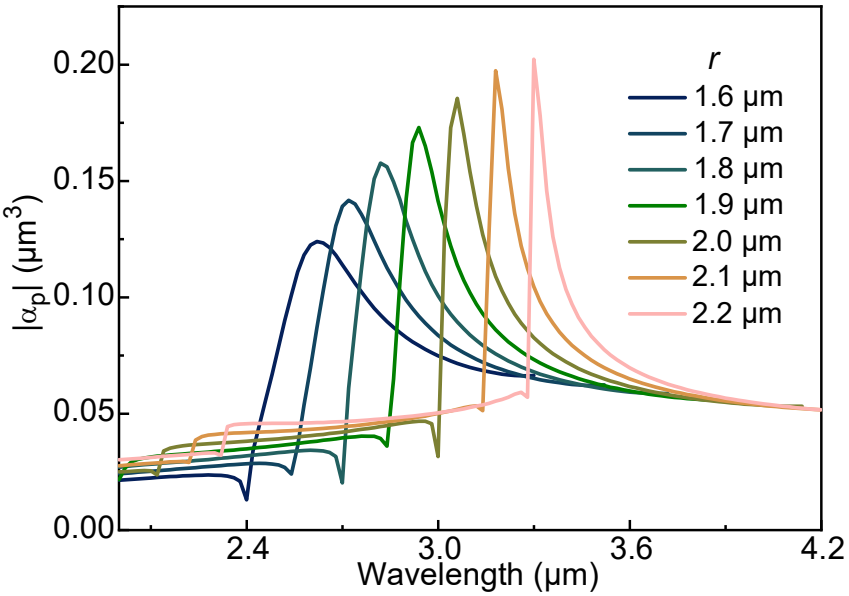

Figure S11. Absolute periodic polarizability $|\alpha_p|$ of square-shaped arrays with different periodic distances *r* = 1.6-2.2 μm, based on acid-treated PEDOT:ToS nanoantennas with 0.80 μm diameter and 0.2 μm height.

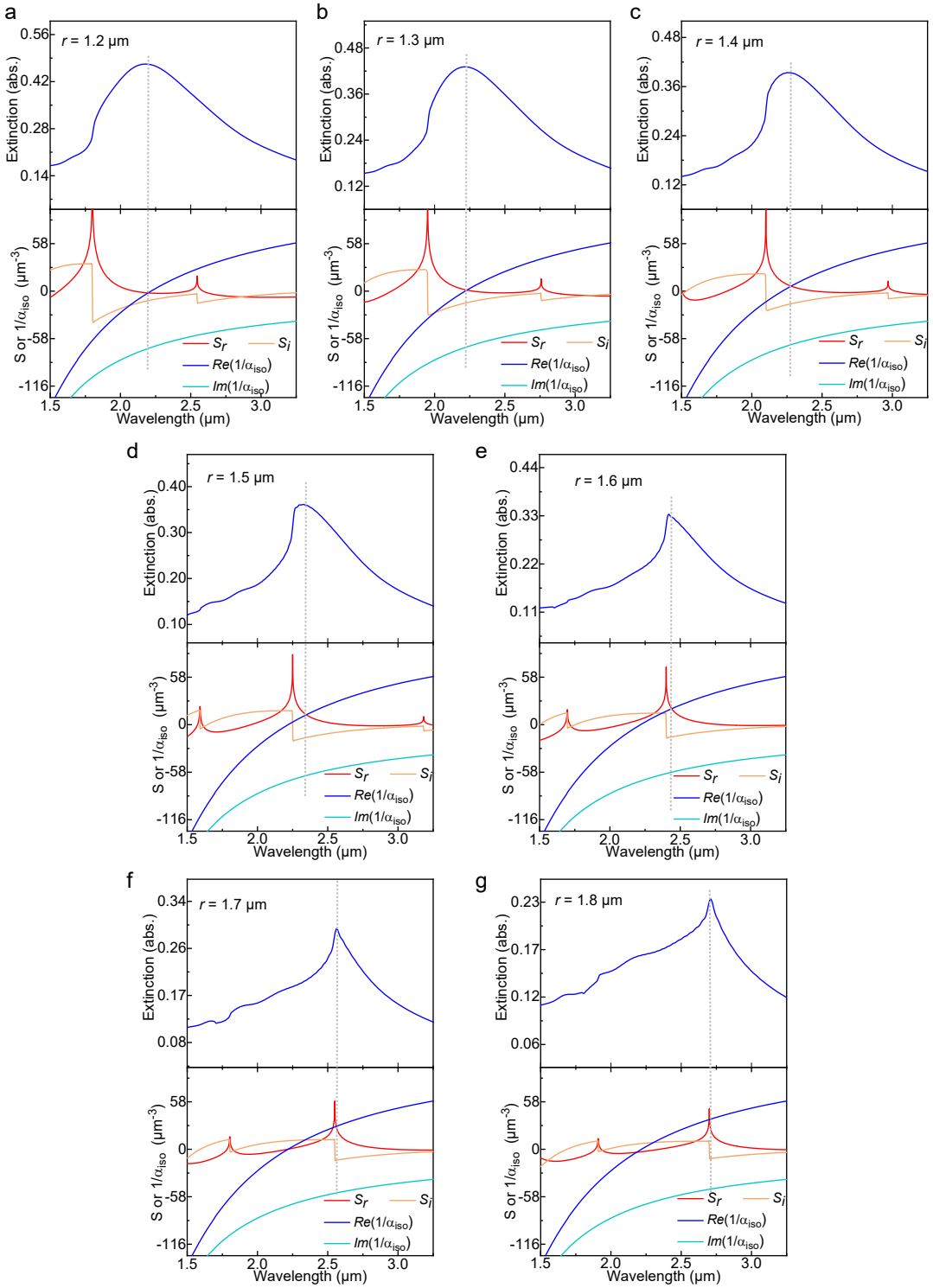

Figure S12. Analysis of array factors and extinction spectra for square arrays with different periodic distances *r* = 1.2-1.8 μm, based on acid-treated PEDOT:ToS. The extinction spectra were obtained by FDTD simulations. The diameter of the nanodisks was set to 0.52 μm, and the height of the nanodisks was set to 0.1 μm.

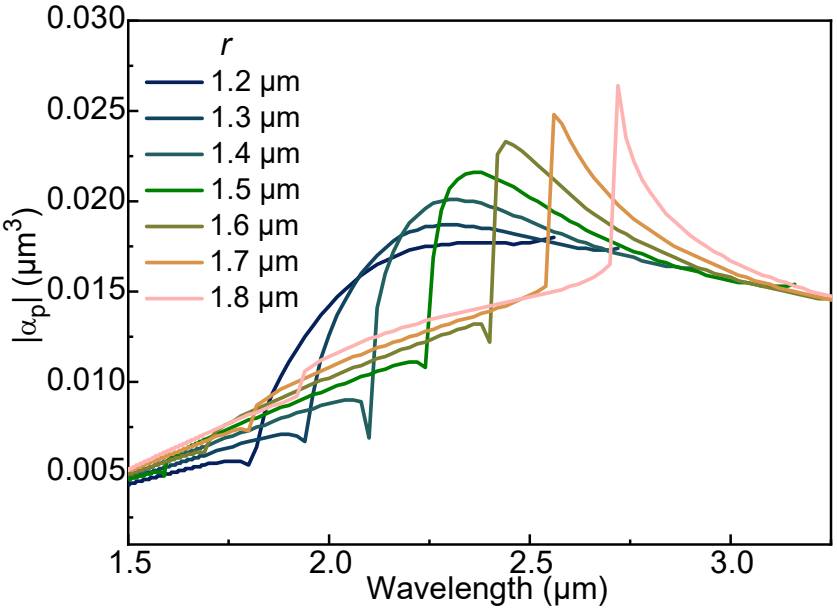

Figure S13. Absolute periodic polarizability $|\alpha_p|$ of square-shaped arrays with different periodic distances *r* = 1.2-1.8 μm, based on acid-treated PEDOT:ToS nanoantennas with 0.52 μm diameter and 0.1 μm height.

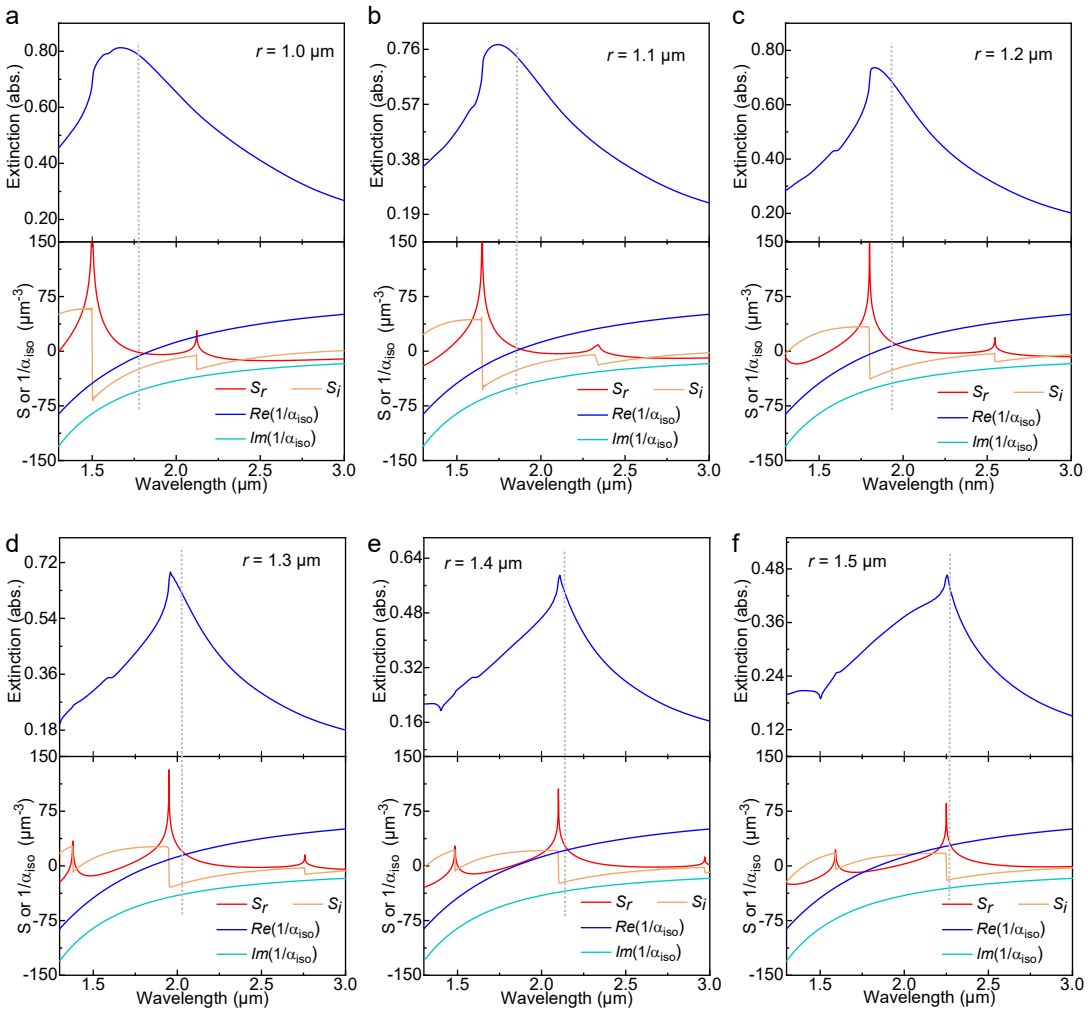

Figure S14. Analysis of array factors and extinction spectra for square arrays with different periodic distances *r* = 1.0-1.5 μm, based on acid-treated PEDOT:ToS. The extinction spectra were obtained by FDTD simulations. The diameter of the nanodisks was set to 0.52 μm, and the height of the nanodisks was set to 0.3 μm.

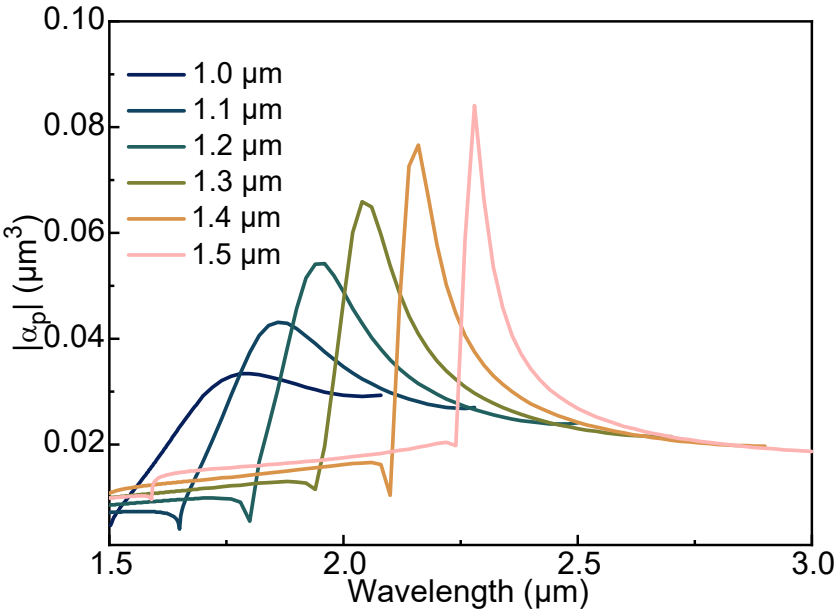

Figure S15. Absolute periodic polarizability $|\alpha_p|$ of square-shaped arrays with different periodic distances *r* = 1.0-1.5 μm, based on acid-treated PEDOT:ToS nanoantennas with 0.52 μm diameter and 0.3 μm height.

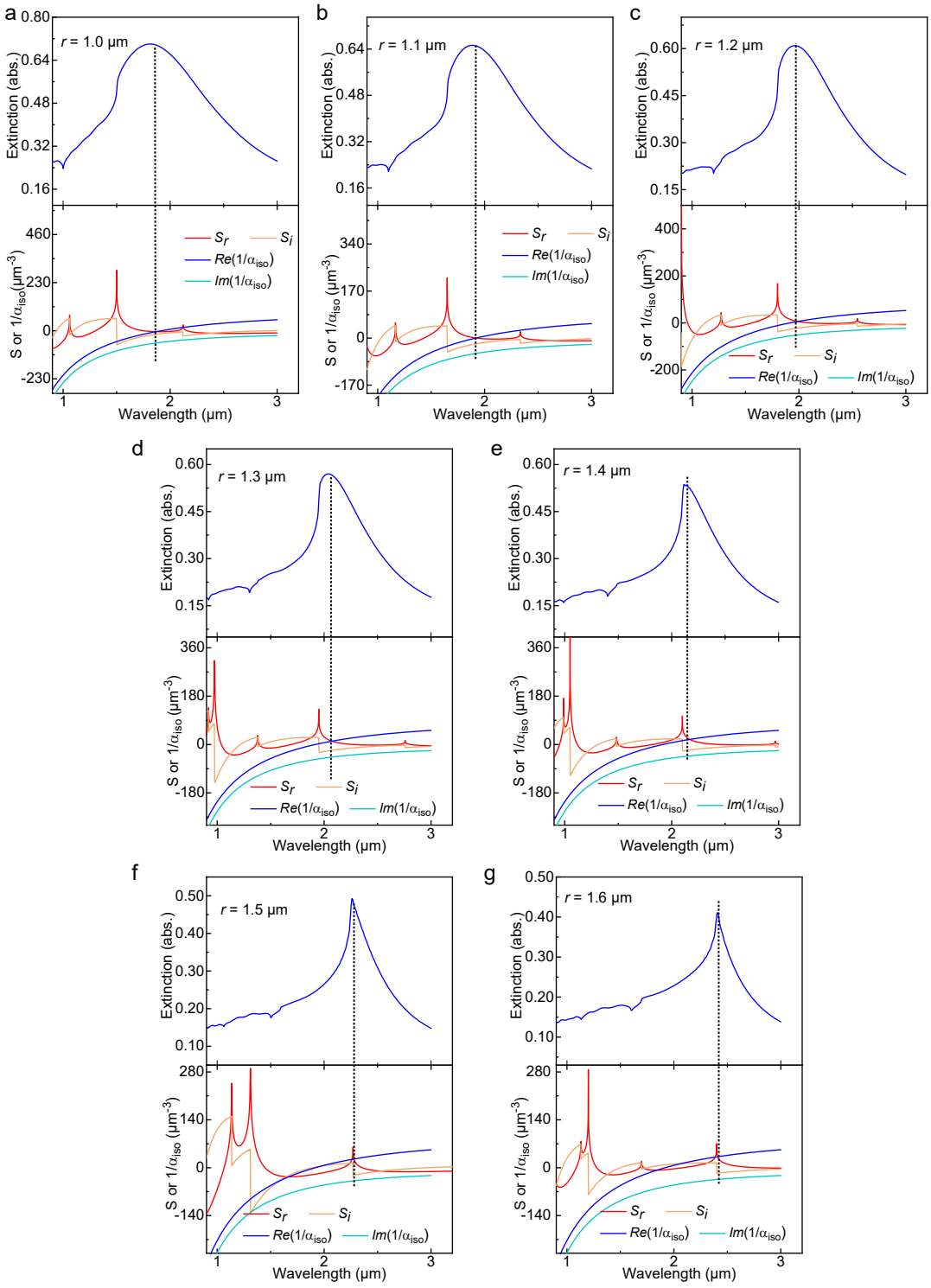

Figure S16. Analysis of array factors and extinction spectra for square arrays with different periodic distances *r* = 1.0-1.6 μm, based on nanoantennas made from PEDOT:Sulf[1]. The extinction spectra were obtained by FDTD simulations. The diameter of nanodisks was set to 0.52 μm, and the height of nanodisks was set to 0.2 μm.

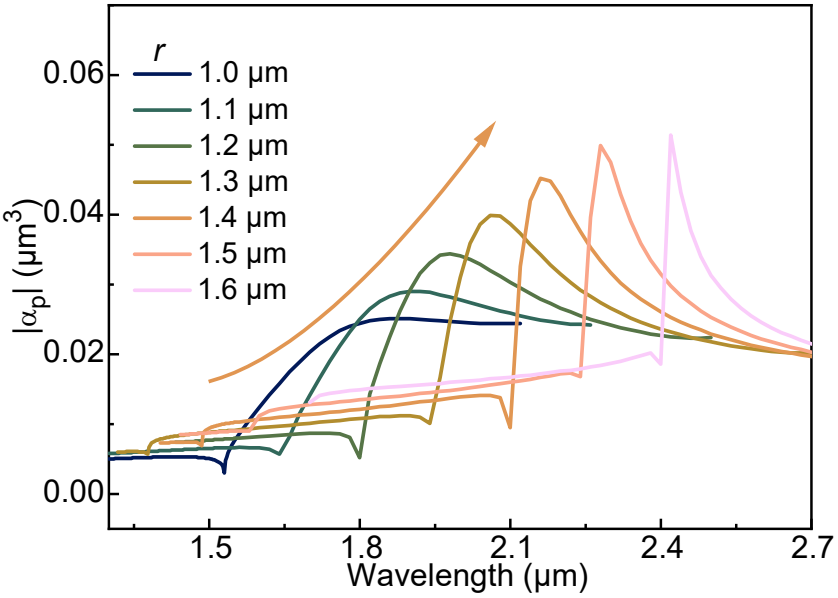

Figure S17. Absolution values of periodic polarizability $|\alpha_p|$ in square-shaped array factors with different periodic distances *r* = 1.0-1.6 μm, based on PEDOT:Sulf[1]. The diameter of nanodisks was set to 0.52 μm, and the height of nanodisks was set to 0.2 μm. These peaks correspond to the surface plasmonic resonance based on the coupling interactions along the square-edges.

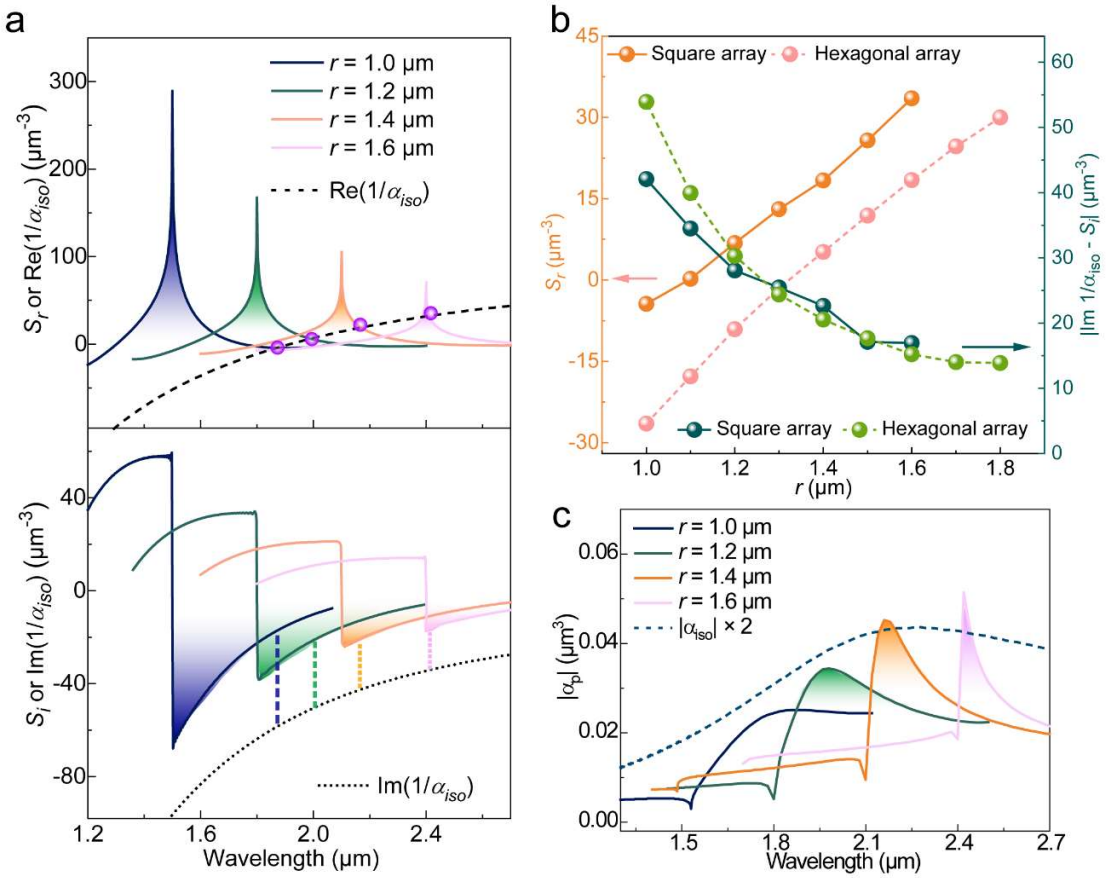

Figure S18. Analysis of matching conditions of CLRs based on nanoantennas made from PEDOT:Sulf[1]. (a) Analysis of the real and imaginary part of array factors (S_r and S_i, respectively) with $1/\alpha_{iso}$, under the periodic distances r = 1.0, 1.2, 1.4, and, 1.6 μm. The diameter of nanodisks was set to 0.52 μm, and the height of nanodisks was set to 0.2 μm. (b) S_r and $|\mathrm{Im}(1/\alpha_{iso}) - S_i|$ at λ_r, in both square and hexagonal arrays. (c) The magnitude of periodic polarizability ($|\alpha_p|$), along with the $|\alpha_{iso}|$ curve from LSPR.

Part 1I: Array factors combined with detuning wavelengths

The calculation of array factors (S) is based on equation S1 (or equation 1 in the manuscript)[2, 3]:

$$S = \sum_j^N \exp(ikr_j)\left[\frac{(1-ikr_j)(3cos^2\theta_j-1)}{r_j^3} + \frac{k^2 sin^2\theta_j}{r_j}\right] \quad \text{S1}$$

where r_j is the central distance between two nanoantennas, θ_j is the angle between the electrical field direction and the lattice vector direction, k is the wave vector ($k = 2\pi n_s/\lambda$) with the wavelength λ, and, N is the number of nanoantennas along the specific direction. In square-shaped arrays, considering the orientation of electrical polarizations decomposed into orthogonal directions (in a random manner), along with the coupling interactions in the diagonal direction of square arrays, the S values are calculated via the equation:

$$S = \sum_j^N \exp(ikr_j)\left\{\left[\frac{(1-ikr_j)[3cos^2\theta_j-1]}{r_j^3} + \frac{k^2 sin^2\theta_j}{r_j}\right] + \left[\frac{(1-ikr_j)[3cos^2(0.5\pi-\theta_j)-1]}{r_j^3} + \frac{k^2 sin^2(0.5\pi-\theta_j)}{r_j}\right]\right\}$$
$$+ \sum_j^N \exp(i\sqrt{2}kr_j)\left\{\left[\frac{(1-i\sqrt{2}kr_j)[3cos^2(0.25\pi-\theta_j)-1]}{2\sqrt{2}r_j^3} + \frac{k^2 sin^2(0.25\pi-\theta_j)}{\sqrt{2}r_j}\right] + \left[\frac{(1-i\sqrt{2}kr_j)[3cos^2(0.75\pi-\theta_j)-1]}{\sqrt{2}r_j^3} + \frac{k^2 sin^2(0.75\pi-\theta_j)}{\sqrt{2}r_j}\right]\right\} \quad \text{(S2)}$$

As $cos^2\theta_j + cos^2(0.5\pi-\theta_j) = sin^2\theta_j + sin^2(0.5\pi-\theta_j) = 1$ and $cos^2(0.25\pi-\theta_j) + cos^2(0.75\pi-\theta_j) = sin^2(0.25\pi-\theta_j) + sin^2(0.75\pi-\theta_j) = 1$, the sin θ_j and cos θ_j parts are eliminated, which simplifies equation S2 to:

$$S = \sum_j^N \{\exp(ikr_j)\left[\frac{(1-ikr_j)}{r_j^3} + \frac{k^2}{r_j}\right] + \exp(i\sqrt{2}kr_j)\left[\frac{(1-ik\sqrt{2}r_j)}{2\sqrt{2}r_j^3} + \frac{k^2}{\sqrt{2}r_j}\right]\} \quad \text{(S3)}$$

At the wavelength of surface plasmonic resonances ($\lambda = \lambda_r$), the wave vector should be:

$$k = \frac{2\pi n_s}{\lambda_r} \quad \text{(S4)}$$

Considering the calculation of normalized detuning wavelength[4] $\Delta = (\lambda_r - n_s r)/n_s r$, where r is the periodic distance, the wave vector can be transformed into equation S5:

$$kr = \frac{2\pi \boldsymbol{nr}}{\boldsymbol{\lambda_r}} = \frac{2\pi}{1+\Delta} \quad \text{(S5)}$$

Thus, the relationship between S and Δ is:

$$S(r,\Delta) = \frac{1}{(Nr)^3}\sum_1^N \{\left[1 - \frac{i2N\pi}{1+\Delta} + \left(\frac{2N\pi}{1+\Delta}\right)^2\right]\exp(\frac{i2N\pi}{1+\Delta}) + \frac{1}{2\sqrt{2}}\left[1 - \frac{i2\sqrt{2}N\pi}{1+\Delta} + \left(\frac{2\sqrt{2}N\pi}{\Delta+1}\right)^2\right]\exp(\frac{i2\sqrt{2}N\pi}{1+\Delta})\} \quad \text{(S6)}$$

According to the Euler equation, the real part of S (denoted as S_r) is:

$$S_r(\Delta, r) = \frac{1}{(Nr)^3}\sum_1^N \{\left[1 + \left(\frac{2N\pi}{1+\Delta}\right)^2\right]\cos\left(\frac{2N\pi}{1+\Delta}\right) + \frac{2N\pi}{1+\Delta}\sin\left(\frac{2N\pi}{1+\Delta}\right) + \frac{1}{2\sqrt{2}}\left[1 + \left(\frac{2N\pi}{1+\Delta}\right)^2\right]\cos\left(\frac{2\sqrt{2}N\pi}{1+\Delta}\right) + \frac{1}{2\sqrt{2}}\frac{2N\pi}{1+\Delta}\sin\left(\frac{2\sqrt{2}N\pi}{1+\Delta}\right)\} \quad \text{(S7)}$$

The imaginary part of S (denoted as S_i) is:

$$S_i(\Delta, r) = \frac{1}{(Nr)^3}\sum_1^N \{[1+\left(\frac{2N\pi}{1+\Delta}\right)^2]\, sin\left(\frac{2N\pi}{1+\Delta}\right) - \frac{2N\pi}{1+\Delta}\cos\left(\frac{2N\pi}{1+\Delta}\right) + \frac{1}{2\sqrt{2}}\left[1+\left(\frac{2N\pi}{1+\Delta}\right)^2\right] sin\left(\frac{2\sqrt{2}N\pi}{1+\Delta}\right) - \frac{1}{2\sqrt{2}}\frac{2N}{1+\Delta}\cos\left(\frac{2\sqrt{2}N\pi}{1+\Delta}\right)\} \quad \text{(S8)}$$

Equations S7 and S8 can be further simplified if neglecting coupling interactions along the diagonal direction[5], and evaluating Δ approximate to 0:

$$S_r(\Delta, r) = \frac{1}{(Nr)^3}\sum_1^N [1+\left(\frac{2N}{1+\Delta}\right)^2] \quad \text{(S9)}$$

$$S_i(\Delta, r) = \frac{1}{(Nr)^3}\sum_1^N(-\frac{2N\pi}{1+\Delta}) \quad \text{(S10)}$$

According to equation S9 and S10, the decrease in Δ can make S_r more positive and S_i more negative, consistent with Figure 2a and 2b in the manuscript, both of which show larger absolution values of array factors that indicates larger coupling interactions between adjacent nanoantennas.

Similarly, hexagonal arrays have an equation of array factor[6] according to:

$$S = \sum_j^N \exp(ikr_j)\left\{\left[\frac{(1-ikr_j)[3cos^2\,\theta_j - 1]}{r_j^3} + \frac{k^2 sin^2\theta_j}{r_j}\right] + \left[\frac{(1-ikr_j)[3cos^2\,(\pi/3-\theta_j)-1]}{r_j^3} + \frac{k^2 sin^2(\pi/3-\theta_j)}{r_j}\right] + \left[\frac{(1-ikr_j)[3cos^2\,(2\pi/3-\theta_j)-1]}{r_j^3} + \frac{k^2 sin^2(2\pi/3-\theta_j)}{r_j}\right]\right\} + \sum_j^N \exp(i\sqrt{3}kr_j)\left\{\left[\frac{(1-i\sqrt{3}kr_j)[3cos^2\,(\pi/6-\theta_j)-1]}{3\sqrt{3}r_j^3} + \frac{k^2 sin^2(\pi/6-\theta_j)}{\sqrt{3}r_j}\right] + \left[\frac{(1-i\sqrt{3}kr_j)[3cos^2\,(\pi/2-\theta_j)-1]}{3\sqrt{3}r_j^3} + \frac{k^2 sin^2(\pi/2-\theta_j)}{\sqrt{3}r_j}\right] + \left[\frac{(1-i\sqrt{3}kr_j)[3cos^2\,(5\pi/6-\theta_j)-1]}{3\sqrt{3}r_j^3} + \frac{k^2 sin^2(5\pi/6-\theta_j)}{\sqrt{3}r_j}\right]\right\} \quad \text{(S11)}$$

The sin θ_j and cos θ_j parts are also eliminated, because $cos^2\,\theta_j + cos^2\,(\pi/3 - \theta_j) + cos^2\,(2\pi/3 - \theta_j) = cos^2\,\theta_j + (\frac{\sqrt{3}}{2}\sin\theta_j + \frac{1}{2}\cos\theta_j)^2 + (\frac{\sqrt{3}}{2}\sin\theta_j - \frac{1}{2}\cos\theta_j)^2 = \frac{3}{2}$ and $cos^2\,(\pi/6 - \theta_j) + cos^2\,(\pi/2 - \theta_j) + cos^2\,(5\pi/6 - \theta_j) = sin^2\,\theta_j + (\frac{1}{2}\sin\theta_j + \frac{\sqrt{3}}{2}\cos\theta_j)^2 + (\frac{1}{2}\sin\theta_j - \frac{\sqrt{3}}{2}\cos\theta_j)^2 = \frac{3}{2}$. Thus, equation S11 can be simplified to:

$$S = \frac{3}{2}[\sum_j^N \exp(ikr_j)(\frac{1-ikr_j}{r_j^3} + \frac{k^2}{r_j}) + \sum_j^N \exp(i\sqrt{3}kr_j)(\frac{1-i\sqrt{3}kr_j}{3\sqrt{3}r_j^3} + \frac{k^2}{\sqrt{3}r_j})] \quad \text{(S11)}$$

At the resonance wavelength $\lambda = \lambda_r$, S can be combined with Δ:

$$S(\Delta, r) = \frac{3}{2}\frac{1}{(Nr)^3}\sum_1^N \{[1 - \frac{i2N\pi}{1+\Delta} + \left(\frac{2N\pi}{1+\Delta}\right)^2]\exp(\frac{i2N\pi}{1+\Delta}) + \frac{1}{3\sqrt{3}}\left[1 - \frac{i3\sqrt{3}N\pi}{1+\Delta} + \left(\frac{3\sqrt{3}N\pi}{\Delta+1}\right)^2\right]\exp(\frac{i3\sqrt{3}N\pi}{1+\Delta})\} \quad \text{(S12)}$$

or when shifting the constant "3/2" to *Nr* part

$$S(r,\Delta) = \frac{1}{(N\sqrt[3]{\frac{2}{3}}r)^3}\sum_1^N \{[1 - \frac{i2N\pi}{1+\Delta} + \left(\frac{2N}{1+\Delta}\right)^2]\exp(\frac{i2N\pi}{1+\Delta}) + \frac{1}{3\sqrt{3}}\left[1 - \frac{i3\sqrt{3}N\pi}{1+\Delta} + \left(\frac{3\sqrt{3}N\pi}{\Delta+1}\right)^2\right]\exp(\frac{i3\sqrt{3}N\pi}{1+\Delta})\} \quad \text{(S13)}$$

In this case, the resonance wavelength λ_r from hexagonal arrays should obey the law (if Δ is approximate to 0):

$$\lambda_r = \sqrt[3]{\frac{2}{3}} n_s r \tag{S14}$$

The simplified S_r and S_i for hexagonal arrays are:

$$S_r(\Delta, r) = \frac{3}{2}\frac{1}{(Nr)^3}\sum_1^N [\,1 + \left(\frac{2N\pi}{1+\Delta}\right)^2\,] \tag{S15}$$

$$S_i(\Delta, r) = \frac{3}{2}\frac{1}{(Nr)^3}\sum_1^N \ (-\frac{2N\pi}{1+\Delta}) \tag{S16}$$

Similar to those in square-shaped arrays, reducing Δ can also increase $|S_r|$ and $|S_i|$ values. However, under the same periodic distance, array factors in hexagonal arrays are around 1.5 times as large as those in square arrays, consistent with stronger coupling interactions[6] from 6 adjacent nanoantennas than coupling interactions from 4 neighboring nanoantennas in square-shaped arrays.

Part 1II: CLR in hexagonal arrays

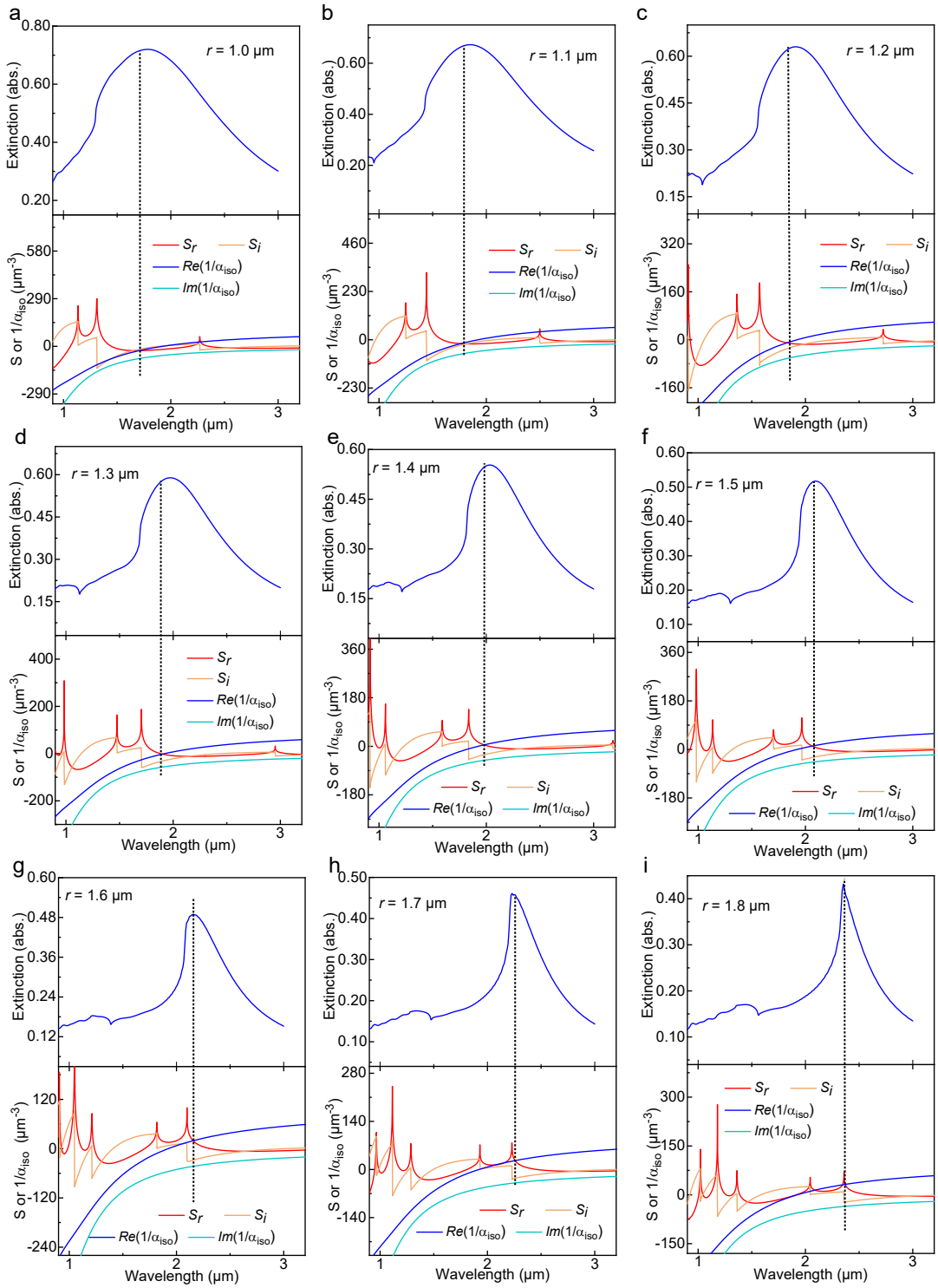

Figure S19. Analysis of factors and extinction spectra in hexagonal arrays with different periodic distances *r* = 1.0-1.8 μm, based on acid-treated PEDOT:ToS. The extinction spectra are

based on the FDTD simulations. The diameter of nanodisks was set to 0.52 μm, and the height of nanodisks was set to 0.2 μm.

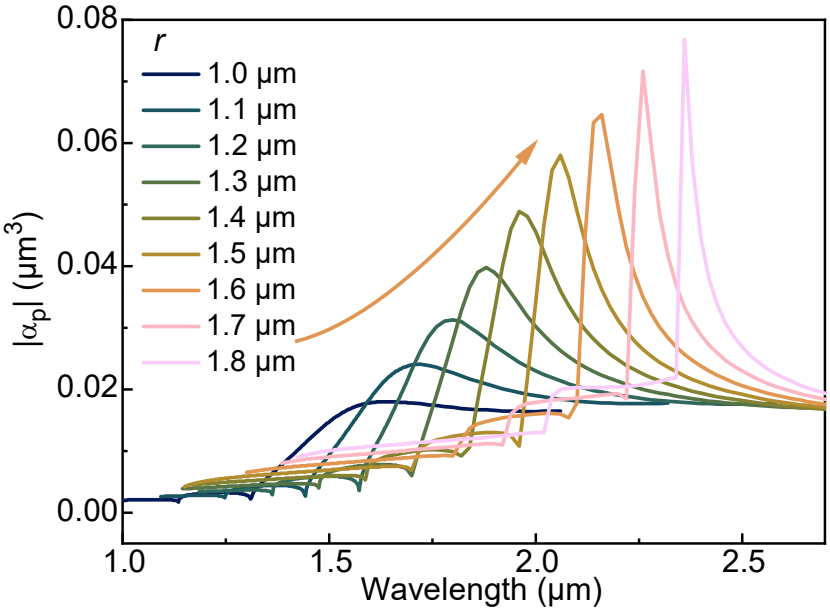

Figure S20. Absolute periodic polarizability $|\alpha_p|$ for hexagonal array with different periodic distances *r* = 1.0-1.8 μm, based on acid-treated PEDOT:ToS. The diameter of nanodisks was set to 0.52 μm, and the height of nanodisks was set to 0.2 μm. These dominant peaks correspond to the surface plasmonic resonance based on the coupling interactions along the hexagonal-edges.

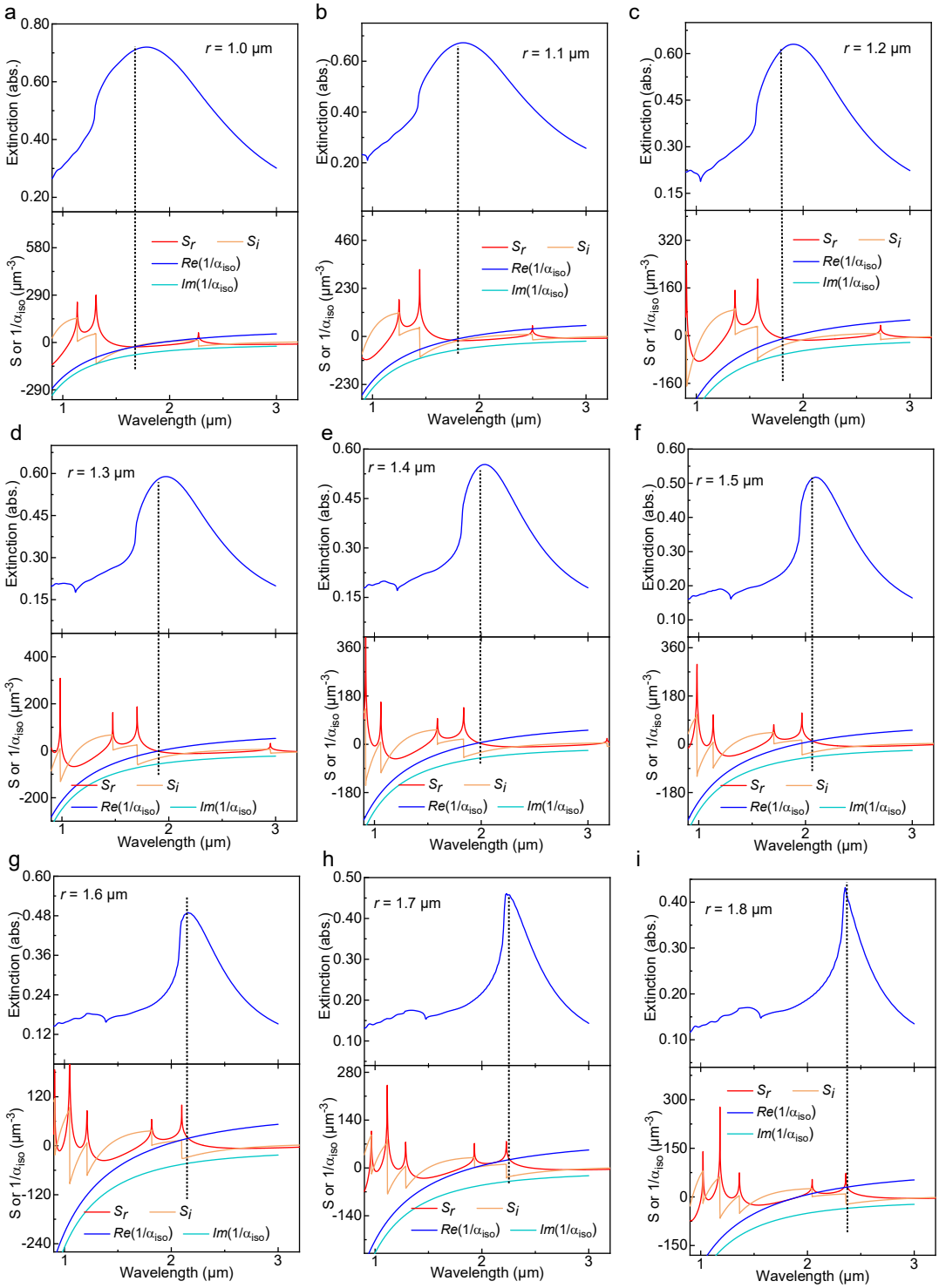

Figure S21. Analysis of factors and extinction spectra in hexagonal arrays with different periodic distances *r* = 1.0-1.8 μm, based on PEDOT:Sulf[1]. The extinction spectra are based on the FDTD simulations. The diameter of nanodisks was set to 0.52 μm, and the height of nanodisks was set to 0.2 μm.

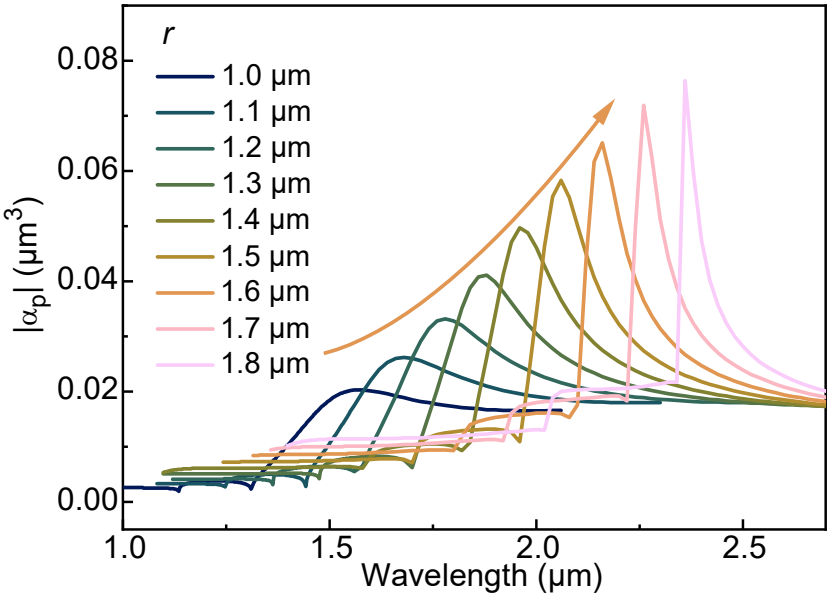

Figure S22. Absolution values of periodic polarizability $|\alpha_p|$ in hexagonal array factors with different periodic distances *r* = 1.0-1.8 μm (calculated from Figure S3), based on PEDOT:Sulf[1]. The diameter of nanodisks was set to 0.52 μm, and the height of nanodisks was set to 0.2 μm. These dominant peaks correspond to the surface plasmonic resonance based on the coupling interactions along the hexagonal-edges.

Part IV. Experimental results of PEDOT-based periodic arrays

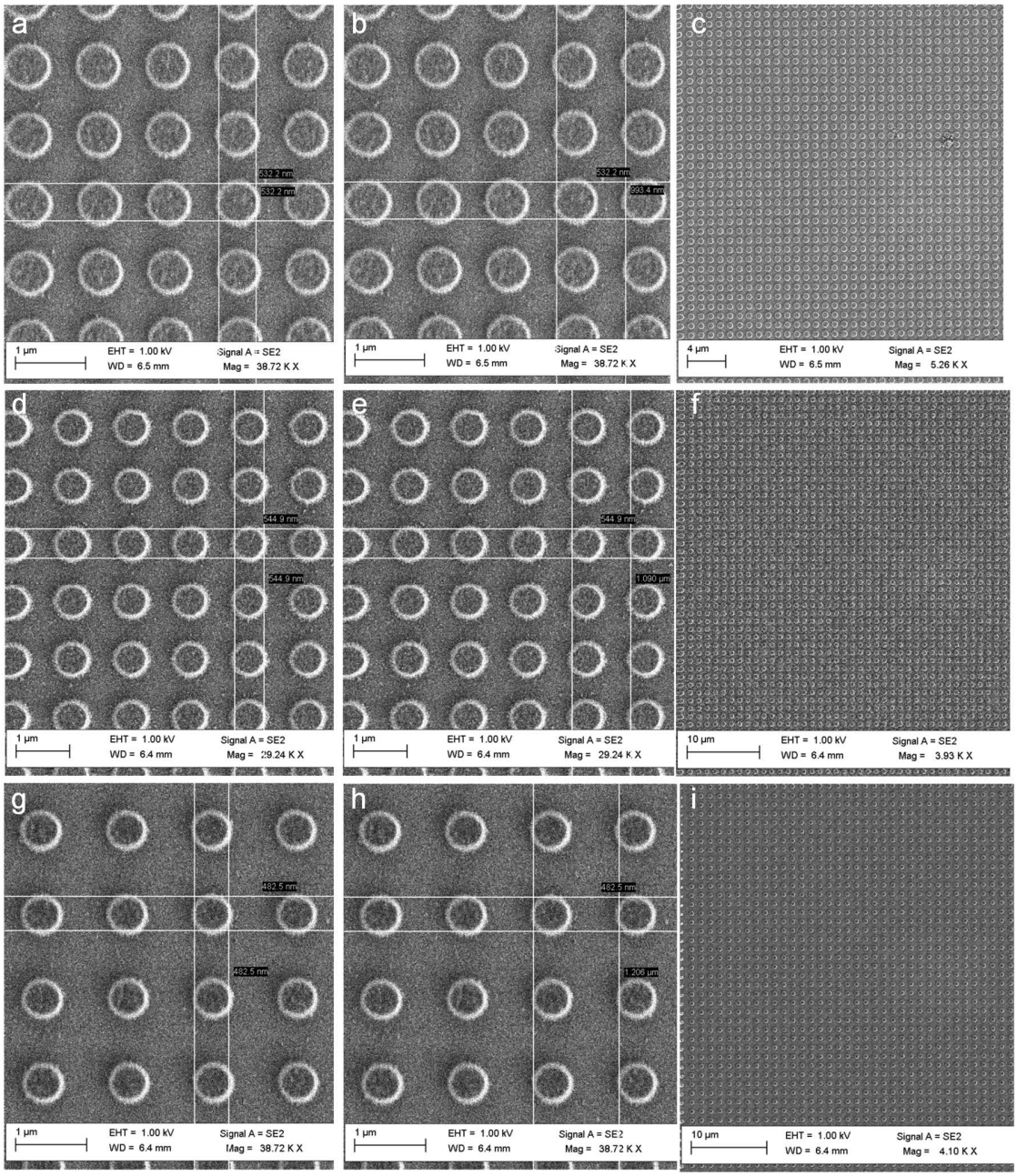

Figure S23. SEM images of PEDOT-based square arrays (r = 1.0~1.2 µm) made through electron beam lithography. (a) (b) (c) for r = 1.0 µm; (d) (e) (f) for r = 1.1 µm; (g) (h) (i) for r = 1.2 µm. The substrate was glass slides and the nanoantenna material was acid-treated PEDOT:ToS.

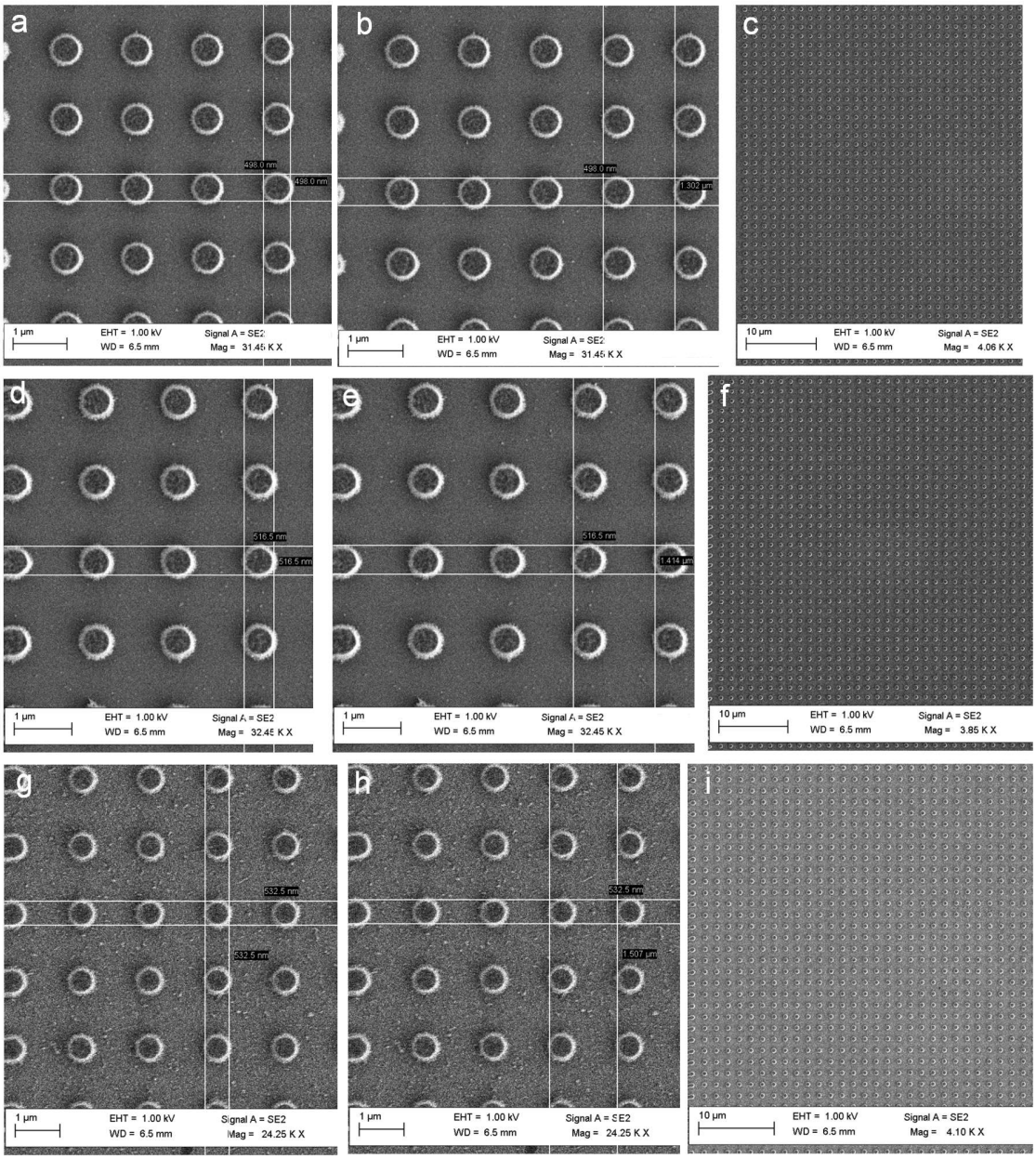

Figure S24. SEM images of PEDOT-based square arrays (r = 1.3~1.5 μm) made through electron beam lithography. (a) (b) (c) for r = 1.3 μm; (d) (e) (f) for r = 1.4 μm; (g) (h) (i) for r = 1.5 μm. The substrate was glass slides and the nanoantenna material was acid-treated PEDOT:ToS.

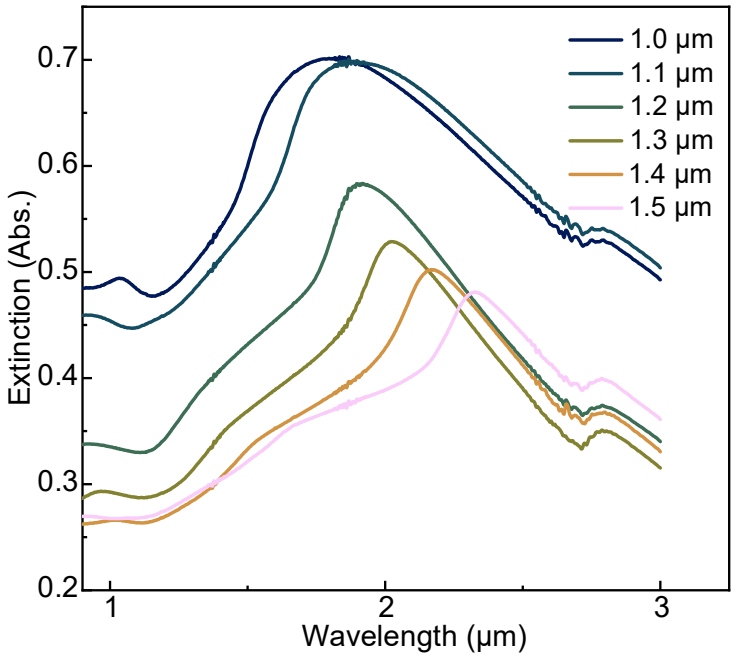

Figure S25. Absolute extinction spectra (experimental results) of PEDOT-based periodic arrays (square shape) with various periodic distances *r* = 1.0~1.5 μm. The nanoantennas were made from acid-treated PEDOT:ToS (the diameters were 0.48-0.54 μm, and the height was 0.2 μm) on glass.

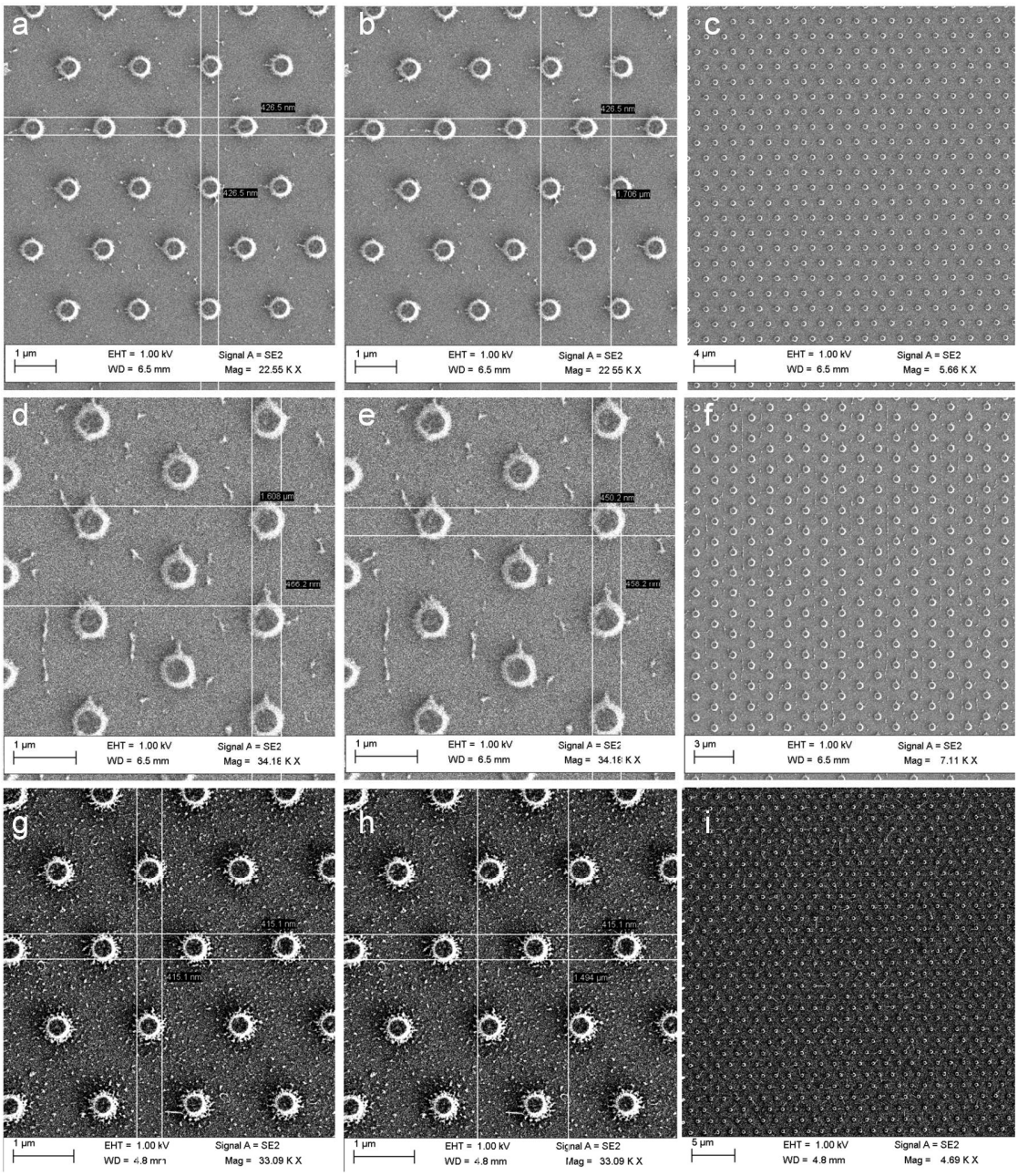

Figure S26. SEM images of PEDOT-based hexagonal arrays (*r* = 1.5~1.7 µm) made through electron beam lithography. (a) (b) (c) for *r* = 1.7 µm; (d) (e) (f) for *r* = 1.6 µm; (g) (h) (i) for *r* = 1.5 µm. The substrate was glass slides and the nanoantenna material was acid-treated PEDOT:ToS. The diameters were 0.48-0.54 µm, and the height was 0.2 µm.

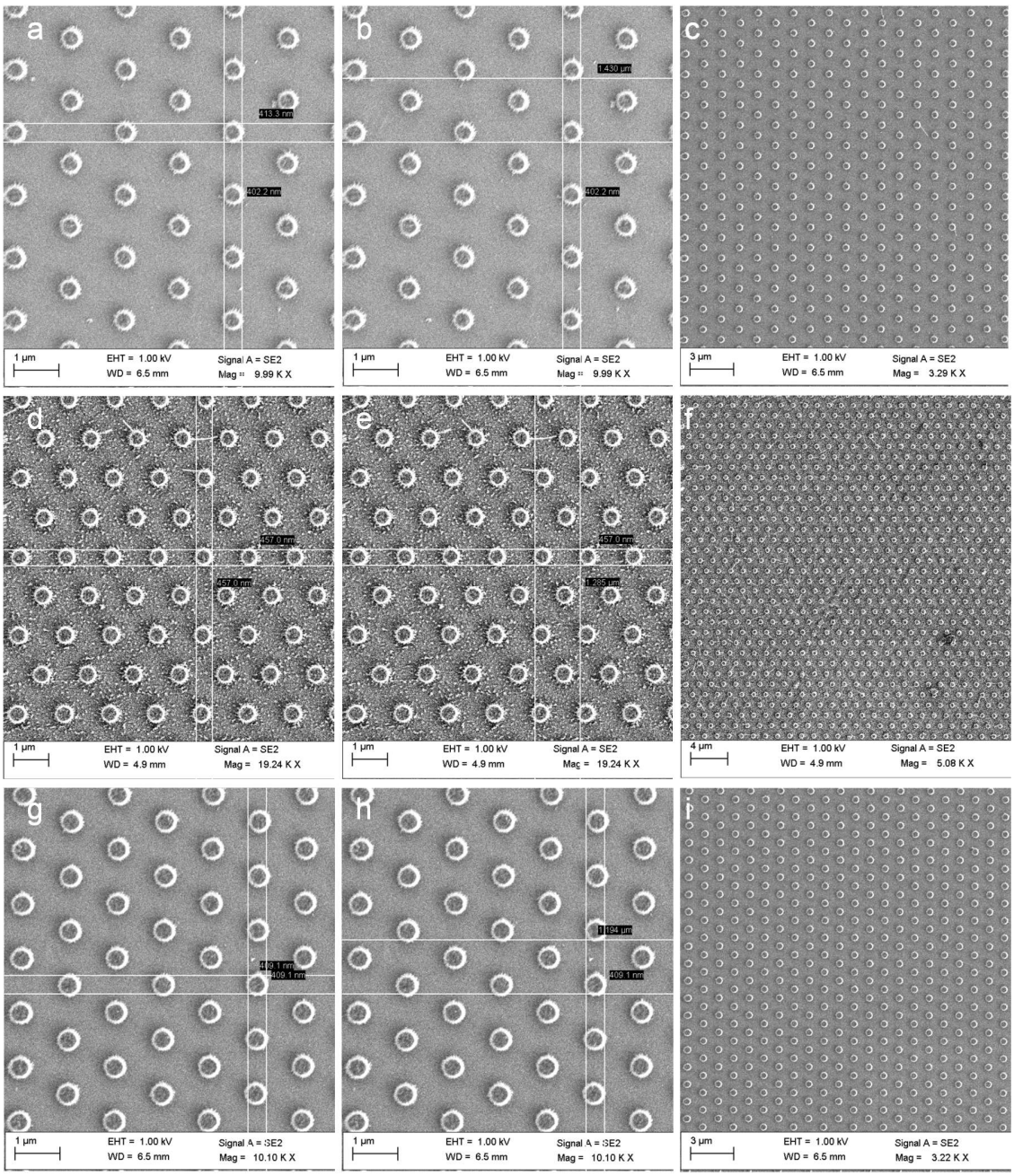

Figure S27. SEM images of PEDOT-based hexagonal arrays (r = 1.2~1.4 µm) made through electron beam lithography. (a) (b) (c) for r = 1.4 µm; (d) (e) (f) for r = 1.3 µm; (g) (h) (i) for r = 1.2 µm. The substrate was glass slides and the nanoantenna material was acid-treated PEDOT:ToS. The diameters were 0.4-0.5 µm, and the height was 0.2 µm.

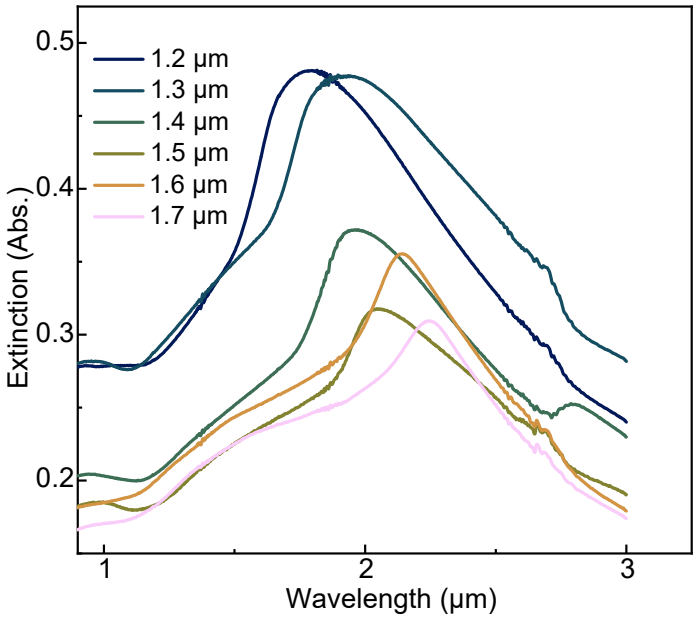

Figure S28. Absolute extinction spectra (experimental results) of PEDOT-based periodic arrays (hexagonal shape) with various periodic distances *r* = 1.2~1.7 μm. The nanoantennas were made from acid-treated PEDOT:ToS (the diameters were 0.4-0.5 μm, and the height was 0.2 μm) on glass.

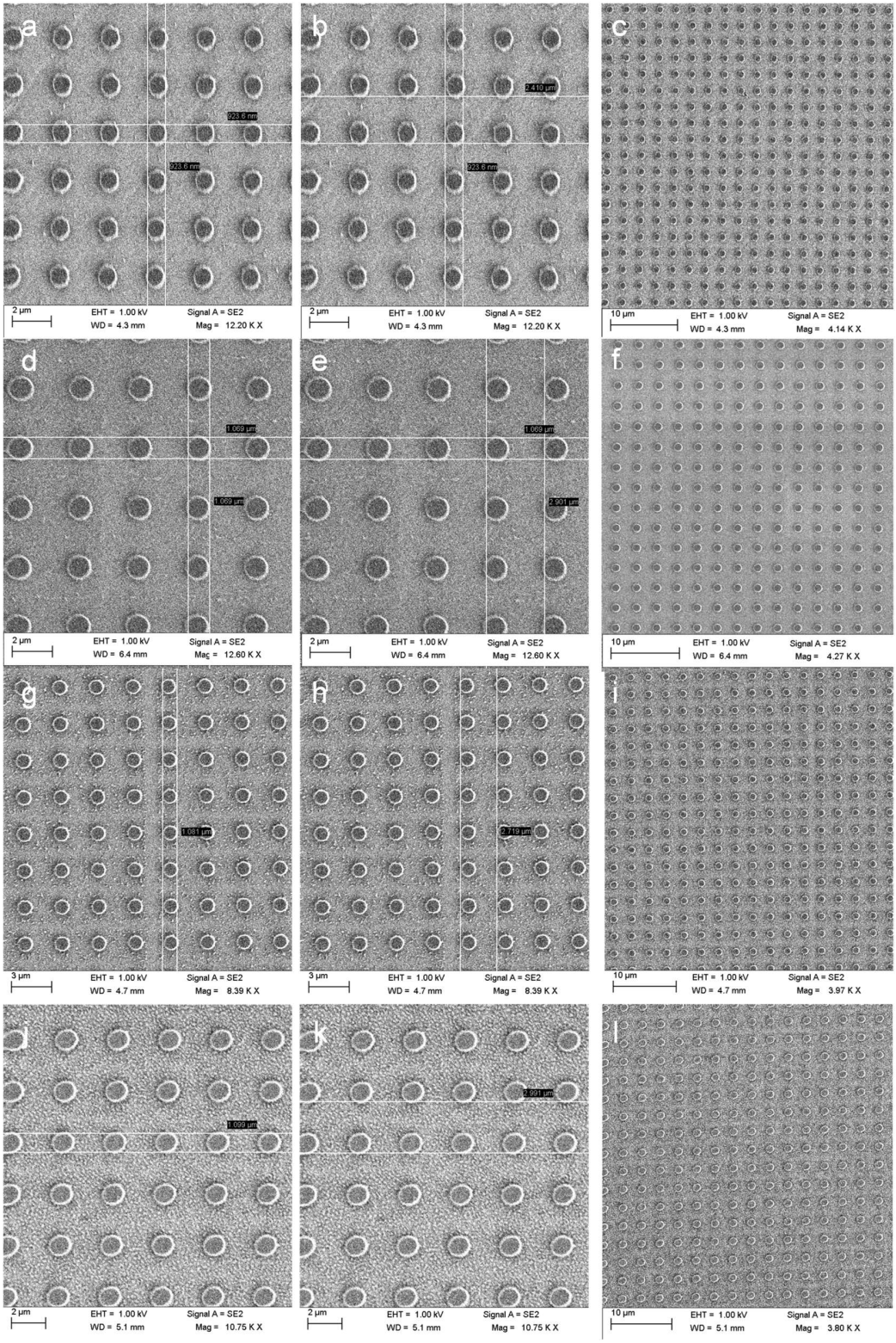

Figure S29. SEM images of PEDOT-based square arrays (r = 2.4~3 µm) made through electron beam lithography. (a) (b) (c) for r = 2.4 µm; (d) (e) (f) for r = 2.7 µm; (g) (h) (i) for r = 2.9 µm; (j) (k)

(l) for r = 3.0 μm. The substrate was CaF_2 slides and the nanoantenna material was acid-treated PEDOT:ToS. The diameters were 0.9-1.1 μm, and the height was 0.2 μm.

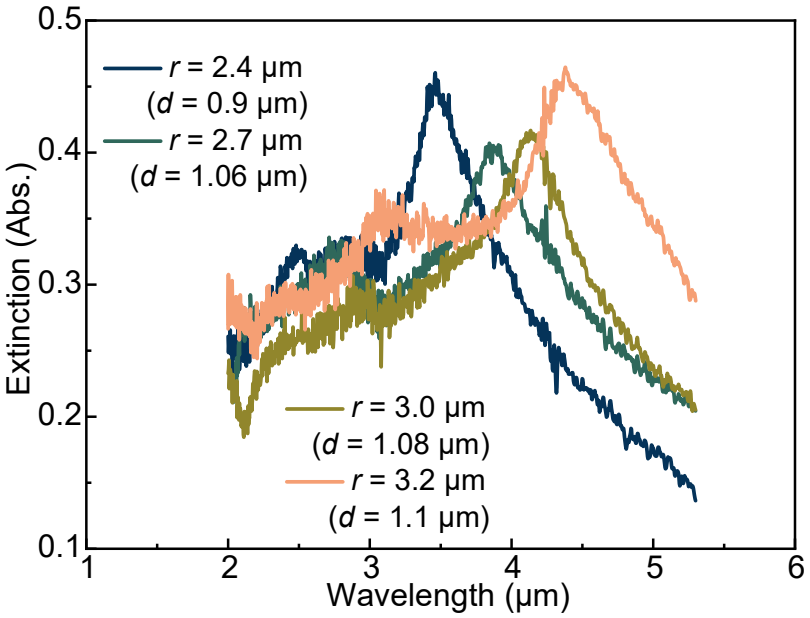

Figure S30. Absolute extinction spectra (experimental results) of PEDOT-based periodic arrays (square shape) with various periodic distances r = 2.4~3.0 μm. The nanoantennas were made from acid-treated PEDOT:ToS (the diameters were 0.9-1.1 μm, and the height was 0.2 μm) on CaF_2 slides.

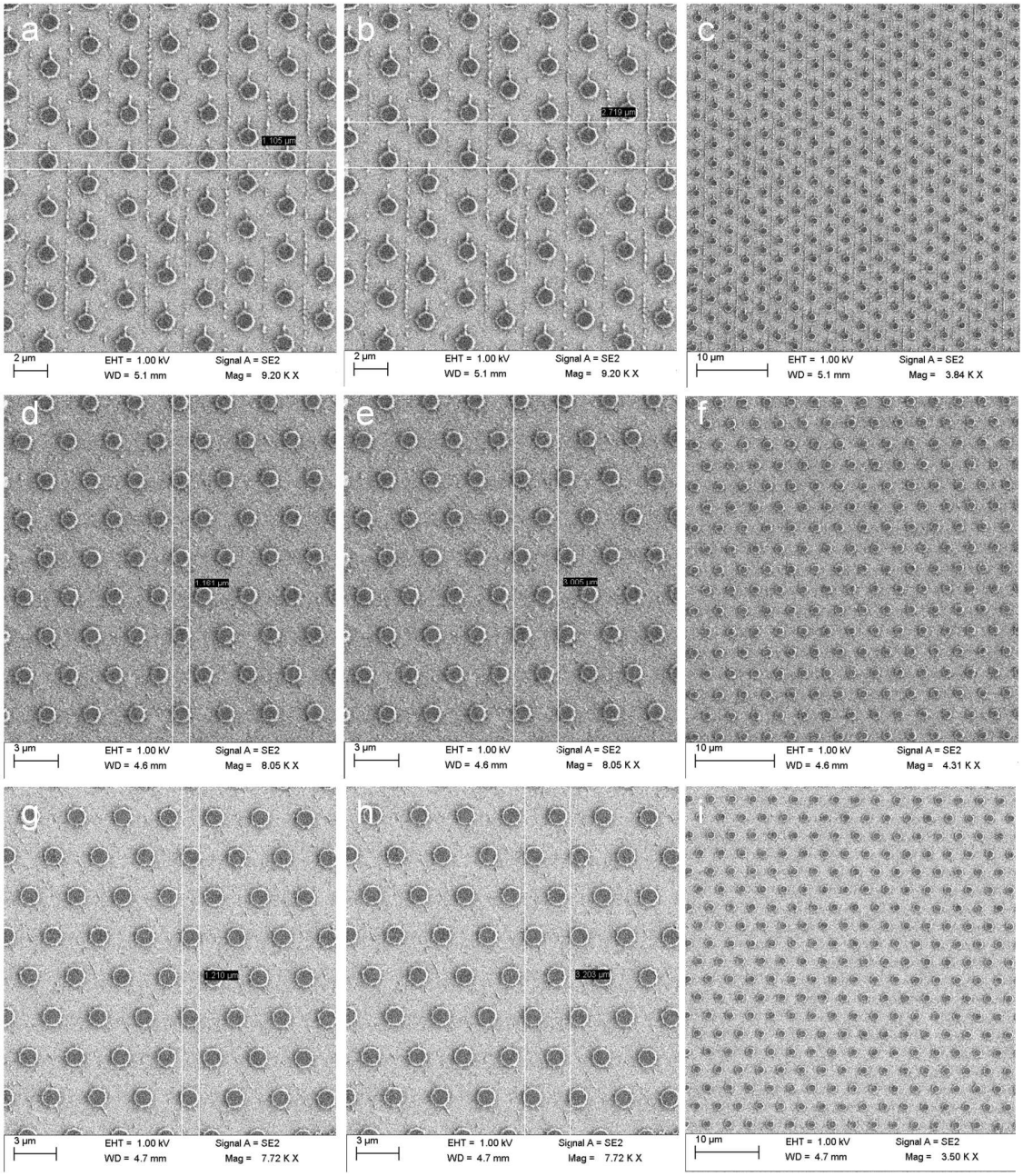

Figure S31. SEM images of PEDOT-based hexagonal arrays (r = 2.7~3.2 µm) made through electron beam lithography. (a) (b) (c) for r = 2.7 µm; (d) (e) (f) for r = 3.0 µm; (g) (h) (i) for r = 3.2 µm. The substrate was CaF_2 slides and the nanoantenna material was acid-treated PEDOT:ToS. The diameters were 1.1-1.2 µm, and the height was 0.2 µm.

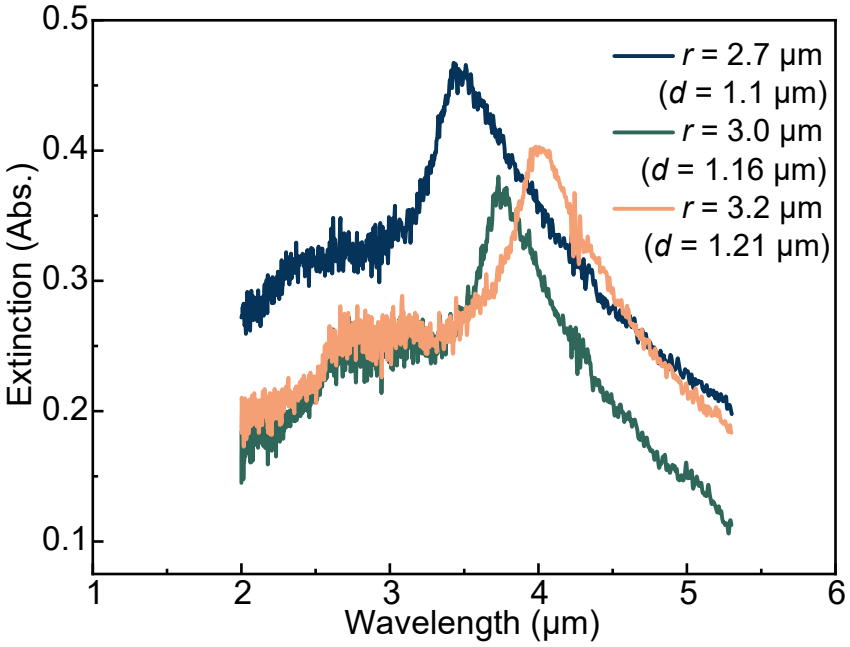

Figure S32. Absolute extinction spectra (experimental results) of PEDOT-based periodic arrays (hexagonal shape) with various periodic distances *r* = 2.7~3.0 μm. The nanoantennas were made from acid-treated PEDOT:ToS (the diameters were 1.1-1.2 μm, and the height was 0.2 μm) on CaF_2 slides.

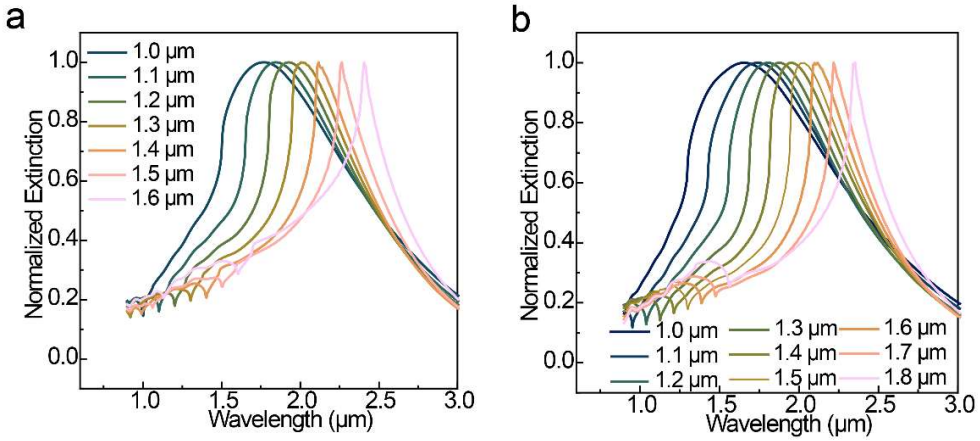

Figure S33. FDTD simulations of *r*-dependent extinction spectra based on PEDOT:Sulf[1]. (a) in square arrays. (b) in hexagonal arrays. The diameter of nanodisks was set to 0.52 μm, and the height of nanodisks was set to 0.2 μm.

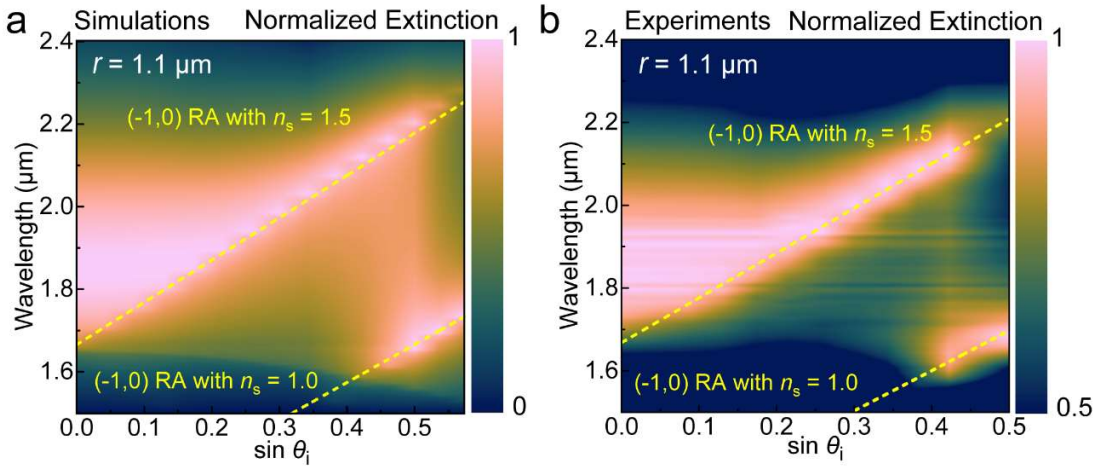

Figure S34. Simulation (a) and experimental results (b) of angle-dependent extinction spectra for a square array with r = 1.1 μm. For FDTD simulations, the diameter of nanodisks was set to 0.52 μm, and the height of nanodisks was set to 0.2 μm. For experimental results, the diameter of nanodisks was 0.54 μm, and the height of nanodisks was 0.2 μm.

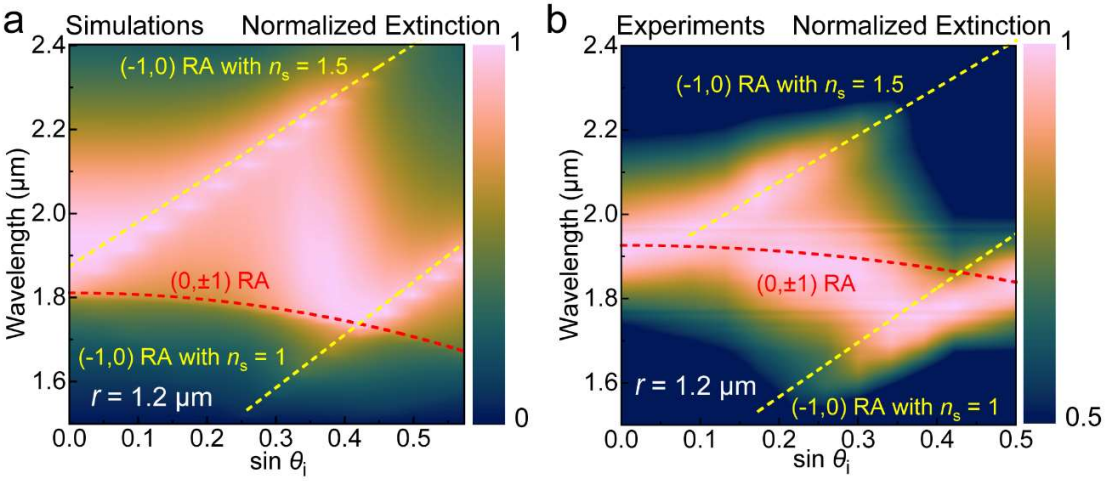

Figure S35. Simulation (a) and experimental results (b) of the angle-dependent extinction spectra under the periodic distance r = 1.2 μm. For FDTD simulations, the diameter of nanodisks was set to 0.52 μm, and the height of nanodisks was set to 0.2 μm. For experimental results, the diameter of nanodisks was 0.48 μm, and the height of nanodisks was 0.2 μm.

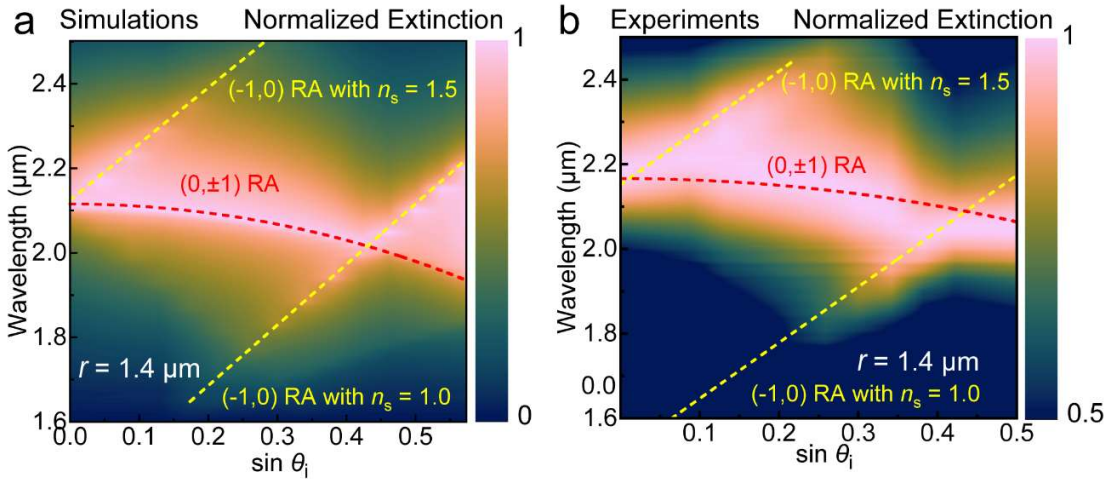

Figure S36. Simulation (a) and experimental results (b) of the angle-dependent extinction spectra under the periodic distance *r* = 1.4 μm. For FDTD simulations, the diameter of nanodisks was set to 0.52 μm, and the height of nanodisks was set to 0.2 μm. For experimental results, the diameter of nanodisks was 0.51 μm, and the height of nanodisks was 0.2 μm.

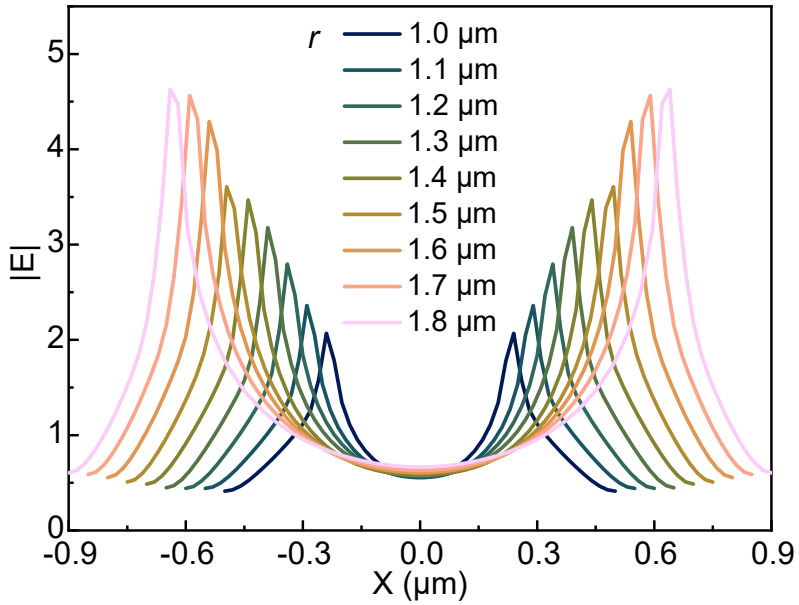

Figure S37. Electrical field distribution for hexagonal arrays with different *r* = 1.0-1.8 μm at λ_r. In these hexagonal arrays, four PEDOT nanoantenna centers locate at the coordinate (X = 0, Y = $\sqrt{3}r/2$), (X = 0, Y = $-\sqrt{3}r/2$), (X = $r/2$, Y = 0), and (X = $-r/2$, Y = 0). At Y = 0, two nanoantenna centers located at X = $\pm r/2$ for respective periodicity. The diameter of PEDOT nanoantennas is set as d = 0.52 μm, and thus the maximum magnitude of electrical field (at hot spot regions) is distributed around X = $r/2 - d/2$ and X = $-r/2 + d/2$. The Z coordinate for electrical field distribution is set at the interface between PEDOT nanoantennas and the dielectric substrate.

Part V. Permittivity in the reduced state

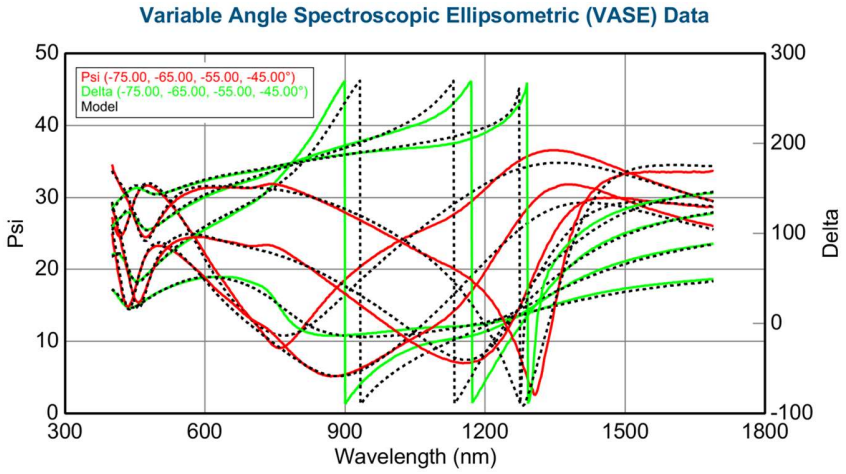

Figure S38. Spectroscopic ellipsometry data (ranging from 210 nm to 1690 nm) for a PEDOT film in the reduced state (achieved by the PEI-treatment of acid-treated PEDOT:ToS). These raw data and the fitting were processed using the VASE software. The Psi (ψ, marked in the red line) and Delta (Δ, marked in the green line) were acquired at four angles (45° , 55° , 65° , and, 75°). The black dashed lines are the best fitting data by using the Drude-Lorents model.

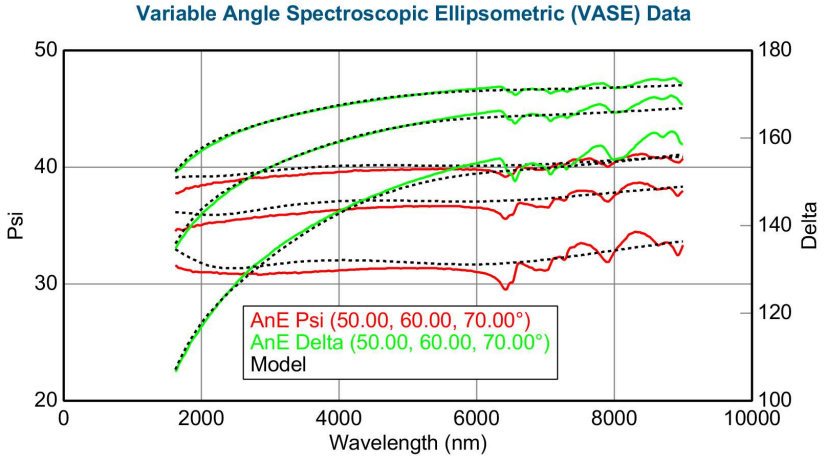

Figure S39. Spectroscopic ellipsometry data (ranging from 1690 nm to 9000 nm) for a PEDOT film in the reduced state (achieved by the PEI-treatment of acid-treated PEDOT:ToS). These raw data and the fitting were processed using the VASE software. The Psi (ψ, marked in the red line) and Delta (Δ, marked in the green line) were acquired at four angles (45° , 55° , 65° , and, 75°). The black dashed lines are the best fitting data by using the Drude-Lorents model.

Supplemental table 3: Oscillators for reduced state in the in-plane direction

$\varepsilon_\infty = 1.50$			
Oscillator No. (j th)	Frequency ω_j (eV)	Broadening γ_j (eV)	Amplitude A_j (eV^2)
1	2.06	0.80	5.73
2	0.021	0.014	0.0059
3	0.020	1.24	0.22
Pole	9.488	0	107.53

Supplemental table 4: Oscillators for reduced state in the out-of-plane direction

$\varepsilon_\infty = 1.50$			
Oscillator No. (j th)	Frequency ω_j (eV)	Broadening γ_j (eV)	Amplitude A_j (eV^2)
1	5.64	0.84	32.60
2	0.018	0.019	0.0070
3	0.018	0.03	0.0090
Pole	10.63	0	24.35

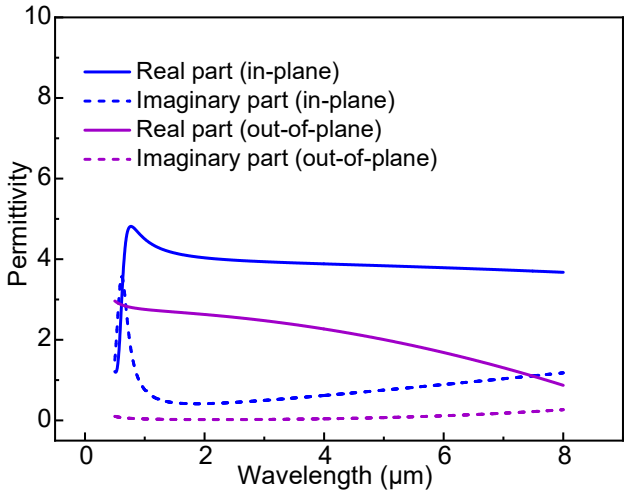

Figure S40. Permittivity of PEDOT film in the reduced state (after PEI treatment and washed by DI water). These data are obtained from the calculation of Drude-Lorentz model by fitting the data of spectroscopic ellipsometry above. The film thickness was around 200 nm.

Part VI. Redox recycles

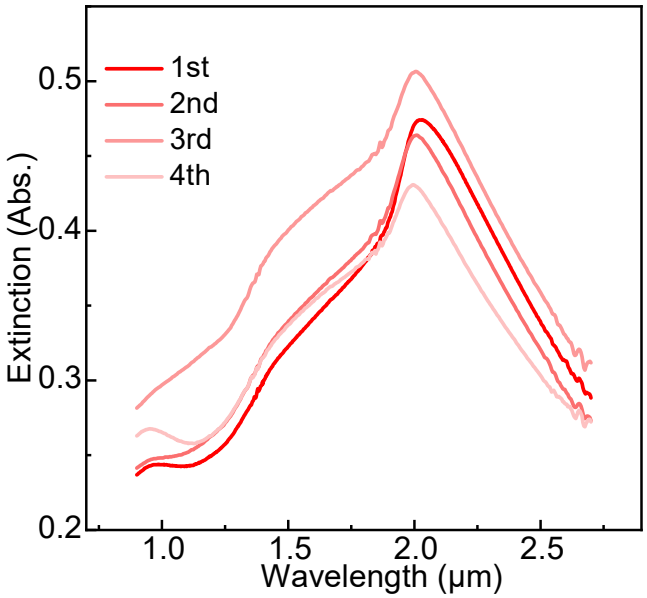

Figure S41. Absolute extinction intensity of collective lattice resonance after 1-4 redox recycles. The diameter of nanodisks was 0.50 μm, and the height of nanodisks was 0.2 μm. The periodic distance is 1.3 μm.

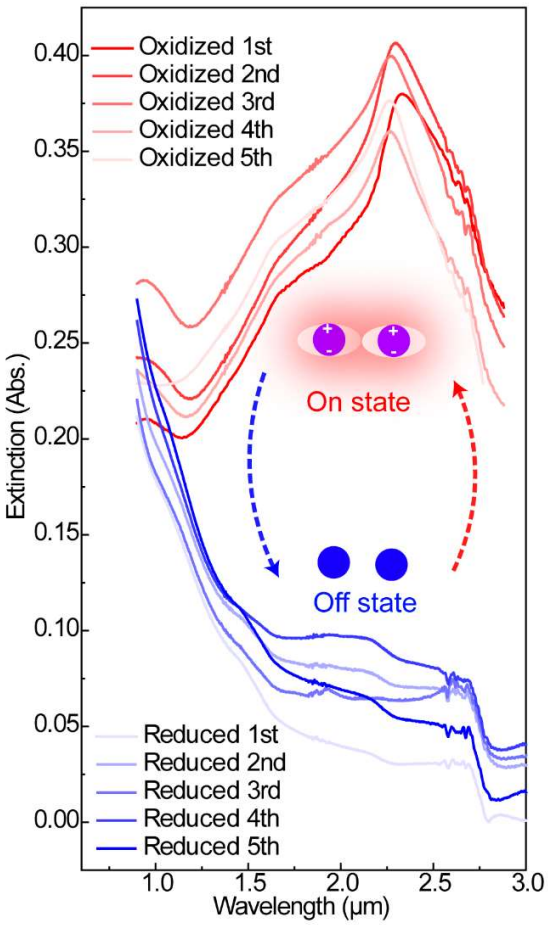

Figure S42. Redox recycle performances of PEDOT-based periodic arrays with *r* = 1.5 μm. The diameter of nanodisks was 0.54 μm, and the height of nanodisks was 0.2 μm.

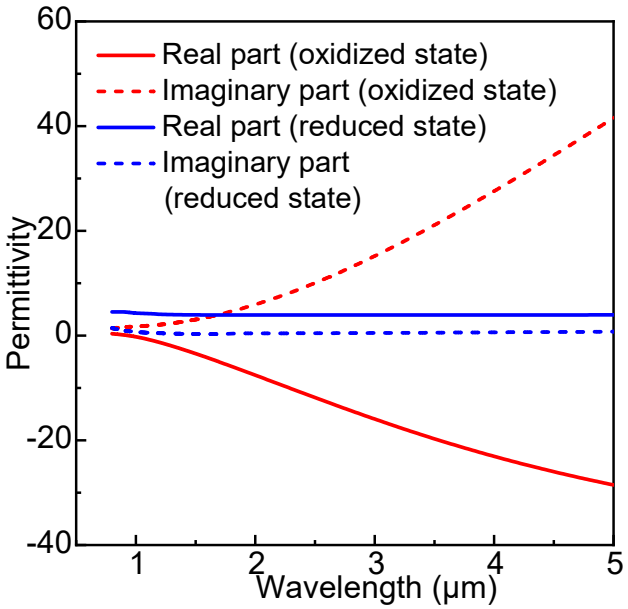

Figure S43. In-plane permittivity dispersion of PEDOT films in different redox states. These data are extracted from Figure S3 and S40 in the wavelength region of 0.8-5 μm. The film thicknesses were about 0.2 μm.

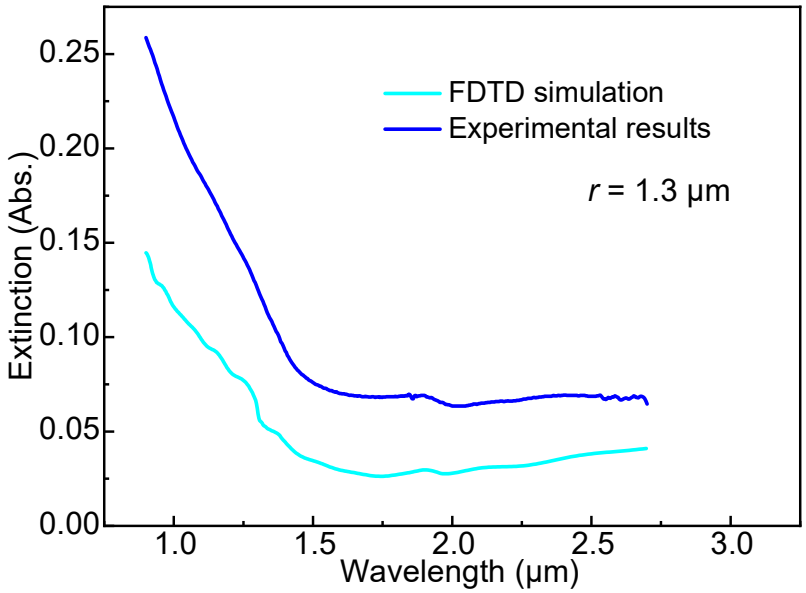

Figure S44. Extinction spectra of PEDOT-based periodic arrays (r = 1.3 μm) in the reductive state. In both FDTD simulations and experimental results, the diameter of nanodisks was 0.5 μm, and the height of nanodisks was 0.2 μm.

References:

1. Chen S*, et al.* Conductive polymer nanoantennas for dynamic organic plasmonics. *Nat. Nanotechnol.* **15**, 35-40 (2020).

2. Humphrey AD, Barnes WL. Plasmonic surface lattice resonances on arrays of different lattice symmetry. *Phys. Rev. B* **90**, 075404 (2014).

3. Auguié B, Barnes WL. Collective Resonances in Gold Nanoparticle Arrays. *Phys. Rev. Lett.* **101**, 143902 (2008).

4. Liang Y, Tsai DP, Kivshar Y. From Local to Nonlocal High-Q Plasmonic Metasurfaces. *Phys. Rev. Lett.* **133**, 053801 (2024).

5. Huttunen MJ, Dolgaleva K, Törmä P, Boyd RW. Ultra-strong polarization dependence of surface lattice resonances with out-of-plane plasmon oscillations. *Opt Express* **24**, 28279-28289 (2016).

6. Guo R, Hakala TK, Törmä P. Geometry dependence of surface lattice resonances in plasmonic nanoparticle arrays. *Phys. Rev. B* **95**, 155423 (2017).